TITLE

Comparative proximity biotinylation implicates RAB18 in cholesterol mobilization and biosynthesis

RUNNING TITLE

GEF-dependent RAB18 interactions

AUTHORS

Robert S. Kiss*[1], Jarred Chicoine[1], Youssef Khalil[2], Robert Sladek[1], He Chen[1], Alessandro Pisaturo[1], Cyril Martin[1], Jessica D. Dale[3], Tegan A. Brudenell[3], Archith Kamath[4,5], Emanuele Paci[6], Peter Clayton[2], Jimi C. Wills[4], Alex von Kriegsheim[4], Tommy Nilsson[1], Eamonn Sheridan[3], Mark T. Handley*[3,7]

AFFILIATIONS

[1]Research Institute of the McGill University Health Centre

1001 boul Decarie

Glen Site Block E

Montreal, QC

H4A 3J1

Canada

[2] Genetics and Genomic Medicine

Great Ormond Street Institute of Child Health

University College London

30 Guilford Street

London

WC1N 1EH

United Kingdom

[3]Leeds Institute of Medical Research

St James's University Hospital

Leeds

LS9 7TF

United Kingdom

[4]Cancer Research UK Edinburgh Centre

MRC Institute of Genetics & Molecular Medicine

The University of Edinburgh

Western General Hospital

Edinburgh

EH4 2XR

United Kingdom

[5]Medical Sciences Division

University of Oxford

Oxford

OX3 9DU

United Kingdom

[6]Astbury Centre for Structural Molecular Biology

University of Leeds

Leeds

LS2 9JT

United Kingdom

[7]Faculty of Biological Sciences

University of Leeds

Leeds

LS2 9JT

United Kingdom.

*authors contributed equally

CORRESPONDING AUTHORS

Robert S. Kiss: robert.kiss@mcgill.ca

Mark T. Handley: m.handley@leeds.ac.uk

KEYWORDS

RAB18, BioID, Cholesterol, Lathosterol, EBP, ORP2

SUMMARY STATEMENT

We used proximity biotinylation together with guanine nucleotide exchange factor (GEF)-null cell lines to discriminate functional RAB18-interactions. This approach revealed that RAB18 mediates lathosterol mobilization and cholesterol biosynthesis.

ABSTRACT

Loss of functional RAB18 causes the autosomal recessive condition Warburg Micro syndrome. To better understand this disease, we used proximity biotinylation in HEK293 and HeLa cells to generate an inventory of potential RAB18 effectors. A restricted set of 25 RAB18-interactions were regulated by the binary RAB3GAP1-RAB3GAP2 RAB18-guanine nucleotide exchange factor (GEF) complex. These included three groups of functionally interrelated proteins: a group of microtubule-interacting/membrane shaping proteins; a group of proteins involved in membrane tethering and docking; and a group of lipid-modifying/lipid transport proteins. We provide confirmatory evidence for several of the interactors (SPG20/SPART, SEC22A, TMCO4). Further we provide functional evidence that RAB18 links the Δ8-Δ7 sterol isomerase emopamil binding protein (EBP) to a molecular machinery mobilizing the products of EBP-catalysis. The cholesterol precursor lathosterol accumulates in RAB18-null cells, and *de novo* cholesterol biosynthesis is reduced. Our data demonstrate that GEF-dependent Rab-interactions are highly amenable to interrogation by proximity biotinylation and suggest that Micro syndrome is a cholesterol biosynthesis disorder.

INTRODUCTION

Rab Proteins are a large subfamily of small GTPases with discrete roles in coordinating membrane trafficking (Zhen & Stenmark, 2015). They associate with cellular membranes as a result of their C-terminal prenylation and like other small GTPases, adopt different conformations and enter into different protein-protein interactions according to whether they are GDP-, or GTP-bound. For Rab proteins, cycles of GTP binding and hydrolysis are accompanied by cycles of membrane association and dissociation that serve to promote the targeting of particular Rab protein isoforms to particular membrane compartments. Although they possess some intrinsic GTP-hydrolysis activity, their *in vivo* nucleotide-bound state is tightly governed in cells by two classes of regulatory proteins. Guanine-nucleotide exchange factors (GEFs) catalyse the exchange of bound GDP for GTP while GTPase-activating proteins (GAPs) promote the hydrolysis of bound GTP to GDP (Barr & Lambright, 2010, Lamber et al., 2019). The dissociation of Rab proteins from membranes is mediated by GDP-dissociation inhibitor (GDI) proteins. GDIs sequester GDP-bound Rabs in the cytosol, and are also involved in their reassociation with membranes (Zhen & Stenmark, 2015).

Rab proteins have a variety of roles in the regulation of processes required to confer compositional identity to membranous organelles and to subdomains within them. These include membrane remodelling and the establishment of membrane contact sites (Bui et al., 2010, Raiborg et al., 2015, Rocha et al., 2009, Sobajima et al., 2018). Where exchange between organelles is mediated by carrier vesicles, these processes are important in vesicle budding and transport, tethering at the appropriate target membrane, and fusion (Cai et al., 2007). Under other circumstances, membrane contact sites may be established to mediate direct fusion between organelles or to facilitate the transfer of lipids and ions (Langemeyer et al., 2018, Wickner, 2010, Wu et al., 2018). Rab proteins fulfil their roles by way of protein-protein interactions with interacting partners termed ‘effectors’. These comprise an array of phylogenetically unrelated protein classes and can serve a range of molecular functions. As such, they are most usually identified biochemically.

Biochemical identification of Rab effectors is challenging; Rab-effector interactions are usually GTP-dependent and are often highly transient. Immunoprecipitation, affinity purification and yeast-2-hybrid approaches have each been used but may be

more or less effective depending on the Rab isoform studied (Christoforidis et al., 1999, Fukuda et al., 2008). One newer approach that has yielded identification of a number of novel interactions is 'BioID' proximity biotinylation utilizing Rab proteins fused to mutant forms of the promiscuous biotin ligase BirA*; the Rab fusion protein biotinylates proximal proteins which are then purified on streptavidin and identified through mass spectrometry (Gillingham et al., 2019, Liu et al., 2018, Roux et al., 2012). Biotin labelling occurs in a relatively physiological context, and prospective effectors can be purified under high stringency conditions. However, a drawback of the technique is that it does not discriminate between close associations resulting from functional protein-protein interactions and those resulting from overlapping localizations.

RAB18 is a ubiquitously expressed ancestral Rab protein that localizes to the *cis*-Golgi, endoplasmic reticulum (ER) and lipid droplets (LDs)(Gerondopoulos et al., 2014, Handley et al., 2015, Martin et al., 2005, Ozeki et al., 2005). Previous work has suggested that it functions in the regulation of lipolysis, and lipogenesis (Martin et al., 2005, Ozeki et al., 2005, Pulido et al., 2011), trafficking between the Golgi and endoplasmic reticulum (ER) (Dejgaard et al., 2008, Handley et al., 2015), ER structure (Gerondopoulos et al., 2014), exocytosis (Vazquez-Martinez et al., 2007) and autophagy (Bekbulat et al., 2018, Feldmann et al., 2017). In order to address how RAB18 coordinates and performs its roles, we used BioID to generate an inventory of its potential effectors. To discriminate functional interactions, we used complementary comparative analyses in HEK293 and HeLa cells. Known RAB18 effectors were more strongly labelled by a fusion of BirA* and wild-type RAB18 than by one incorporating an inactive form, RAB18(Ser22Asn), which is deficient in nucleotide-binding. Similarly, BirA*-RAB18 labelled known effectors more strongly in wild-type cells than in cells in which RAB18-GEF activity was disrupted with CRISPR. Interestingly, disruption of different GEF complexes largely affected different sets of RAB18 interactions.

Biallelic loss-of-function variants in *RAB18* or in the genes encoding the 'RAB3GAP' RAB18-GEF complex cause the autosomal recessive condition Warburg Micro syndrome (Aligianis et al., 2005, Bem et al., 2011, Borck et al., 2011, Handley & Sheridan, 2018, Liegel et al., 2013)(MIMs 600118, 614222, 614225, 615663, 212720). We found that a restricted set of RAB18-interactions were RAB3GAP-

dependent, including known and novel effectors in three functional groups. We present direct validation for several examples including the microtubule-binding protein SPG20/SPART, the SNARE protein homologue SEC22A and an orphan lipase TMCO4. Our data strongly support a previous suggestion (Xu et al., 2018) that RAB18 effectors act collectively in lipid transfer between closely apposed membranes. Further, we provide evidence that RAB18 serves to coordinate the generation of the cholesterol precursor lathosterol by the EBP enzyme and its subsequent mobilization by the lipid transfer protein (LTP) ORP2/OSBPL2. Because of the clinical overlap between Micro syndrome and conditions including lathosterolosis (MIM 607330) and Smith-Lemli-Opitz syndrome (SLOS; MIM 270400), our data suggest that impaired cholesterol biosynthesis may partly underlie Micro syndrome pathology.

RESULTS

An inventory of nucleotide-binding-dependent RAB18-associated proteins in HEK293 cells

We first generated HEK293 cells stably expressing BirA*-tagged fusion proteins of wild-type RAB18, nucleotide-binding deficient RAB18(Ser22Asn) or GTP-hydrolysis deficient RAB18(Gln67Leu) using the Flp-In system (Figure S1). We then carried out proximity-labelling, affinity purification and mass spectrometry of biotinylated proteins as previously described (Roux et al., 2018, Roux et al., 2012). Following removal from the dataset of previously identified non-specific binders from an in-house database, a total of 98 proteins were identified as associating with RAB18 across all samples (see Table S1).

The most comprehensive annotation of candidate RAB18 effectors thus far was made in the 2014 paper by Gillingham et al., which utilized an affinity purification-mass spectrometry (AP-MS) approach and the *Drosophila* RAB18 orthologue (Gillingham et al., 2014). In that study, a total of 456 proteins were identified as interacting with RAB18. However, only 14 of these were well represented in terms of spectral counts, exhibited low non-specific binding to GST/Sepharose and showed low binding to other Rab protein isoforms. We took these 14 proteins as the most plausible physiological RAB18 interactors. Orthologues of 7 of these 14 proteins were also represented in our BioID data. The number of spectral counts recorded for these 7 proteins did not clearly distinguish them from the remainder of this BioID dataset. We therefore proceeded by comparing their differential labelling by the different RAB18 fusion proteins.

We began analyses by exploring the possibility that BirA*-RAB18(Gln67Leu) fusion protein would produce enhanced biotinylation of RAB18-effectors (as compared to BirA*-RAB18(WT)). We normalized total spectral counts between the BirA*-RAB18(Gln67Leu) and BirA*-RAB18(WT) datasets and then calculated mutant:wild-type ratios for each RAB18-associated protein (Table S1). Association ratios for known RAB18-interactors ranged from 0.1-1.49 indicating that RAB18 associations were altered by the Gln67Leu variant, but not predictably so.

We next compared the BirA*-RAB18(Ser22Asn) and BirA*-RAB18(WT) datasets (Figure 1, Table S1). The RAB18-GEF subunits RAB3GAP1 and RAB3GAP2 showed association ratios >1 consistent with the high affinity of Rab-GEFs for cognate Rabs in their nucleotide-free state. Since most effector-interactions are GTP-dependent, we ranked other prospective RAB18-interactors according to those that showed the lowest association ratios. Figure 1B shows the 28 of 98 proteins with BirA*-RAB18:BirA*-RAB18(Ser22Asn) association ratios <0.5. These include the remaining 5 common interactors from the Gillingham et al. study, several of which have association ratios of zero, indicating that labelling by BirA*-RAB18(Ser22Asn) was absent. These data suggest that comparison of labelling by wild-type and nucleotide-binding-deficient BirA*-Rab fusion proteins can be an effective means to distinguish putative effectors.

An inventory of RAB18-GEF-dependent RAB18-associated proteins in HeLa cells

We had previously used CRISPR to generate a panel of clonal, otherwise isogenic, HeLa cell lines, null for RAB18 and a number of its regulators (see Figure S2). Having shown that the BirA*-RAB18(WT):BirA*-RAB18(Ser22Asn) comparison in HEK293 cells was informative, we carried out similar comparisons between BirA*-labelling in wild-type and RAB18-GEF deficient HeLa cells (Figure 2A). Since GEF activity promotes Rab GTP binding, and this is usually necessary for effector interactions, these interactions will be attenuated in GEF-null cells. RAB3GAP1 and RAB3GAP2 are each essential subunits of a binary RAB18-GEF complex whereas TRAPPC9 is reported to be essential for the RAB18-GEF activity of a different GEF, the multisubunit TRAPPII complex (Gerondopoulos et al., 2014, Li et al., 2017). We therefore carried out proximity labelling using transient expression of the same exogenous BirA*-RAB18 construct in wild-type cells and in RAB3GAP1-, RAB3GAP2- and TRAPPC9-null cell lines.

Prior to mass-spec analysis, samples from each of the streptavidin pull-downs were subjected to Western blotting to ensure comparable BirA*-RAB18 expression (Figure S3A). Label-free quantitative proteomics analyses were used to calculate ‘LFQ intensities’ (Cox et al., 2014) for each RAB18-associated protein, which were then normalized in each experiment according to the quantity of RAB18 found in each

sample. Samples from three independent experiments were analysed, and pull-down samples from untransfected biotin-treated cells were used as controls in each case. After filtering the data to remove known mass-spec contaminants, and any protein identified at a high level in control samples, a total of 584, 483 and 506 RAB18-associated proteins were identified in each experiment. A total of 457 proteins were present in two or more of the replicate experiments (see Table S2). Orthologues of 10 of the 14 putative RAB18-interacting proteins identified by Gillingham et al. were identified in the HeLa cell BioID dataset including all 7 of those also identified in the HEK293 cell dataset. However, as in that dataset, these were not distinguished by their comparative abundance.

Different Rab-GEF complexes may operate in distinct subcellular localizations and coordinate associations with different effectors (Carney et al., 2006). Therefore, we assessed whether non-zero intensities for each RAB18-associated protein correlated between samples (Figure 2B, Figure S3B). Very strong correlations between protein intensities from RAB3GAP1- and RAB3GAP2-null cells indicated that loss of either protein had a functionally equivalent effect (R^2=0.99, see Figure 2B). In contrast, intensities from RAB3GAP1- and TRAPPC9-null cells were much more poorly correlated (R^2=0.73, see Figure S3B). We therefore considered RAB3GAP- and TRAPPC9-dependent RAB18-associations separately.

Of the 457 proteins identified in two or more independent experiments, only 25 showed an association ratio <0.5 in the absence of functional RAB3GAP (Figure 2C-D, Table S2). These included orthologues of 9 of the 10 proteins identified in the Gillingham et al. study. Thus, our approach was extremely powerful in discriminating putative effector proteins. 133 proteins showed an association ratio <0.5 in the absence of functional TRAPPC9 including the remaining common RAB18-interactor from the Gillingham et al. study (see Table S2). There was only limited overlap between RAB3GAP- and TRAPPC9-dependent associations (Figure 2C). Indeed, among the 28 nucleotide-binding-dependent RAB18 associations identified in HEK293 cells, 6 were also RAB3GAP-dependent, and 7 were TRAPPC9-dependent in HeLa cells respectively, but none were both (Figure 1B). Among the 25 RAB3GAP-dependent associations in HeLa cells, only 5 were also TRAPPC9 dependent (Figure 2C, Table S2).

One of the TRAPPC9-dependent RAB18 associations was that with TBC1D5, a Tre-2/Bub/Cdc16 (TBC) domain-containing RAB-GAP with a well characterised role in regulation of RAB7 (Jia et al., 2016, Jimenez-Orgaz et al., 2018, Seaman et al., 2009). This was a strong candidate as a RAB18 regulator or effector since it had also been identified in the HEK293 dataset as well as in several previous studies (Gillingham et al., 2019, Gillingham et al., 2014). We generated TBC1D5-null HeLa cells, and first tested whether RAB7 and RAB18 dynamics were altered in these cells using fluorescence recovery after photobleaching (FRAP). RAB7 dynamics were substantially different in the TBC1D5-null cells as compared to those in wild-type cells, consistent with reduced RAB7 GTP-hydrolysis resulting in its reduced GDI-mediated exchange between membrane and cytosolic compartments (Figure S4A). In contrast, RAB18 dynamics were unchanged in TBC1D5-null cells compared to controls (Figure S4B). Further, RAB7 dynamics were unchanged in RAB18-null cells compared to controls, indicating that RAB18 is not required for TBC1D5 activity (Figure S4A). These data do not exclude TBC1D5 as a potential RAB18 effector, but argue against a role for RAB18 in RAB7-regulation under resting conditions.

Validation screening of RAB3GAP-dependent RAB18 associations

Our continued study focused on the 25 RAB3GAP-dependent RAB18 associations identified in HeLa cells on the basis that these included the majority of known RAB18 effectors together with a number of promising candidate effectors not previously identified. Encouragingly, many of these also appeared to share interconnected functions and fell into three main groups (Figure 2D). A group of proteins involved in membrane shaping, cytoskeletal remodelling and in membrane-microtubule contacts included SPG20, BICD2, REEP4, CAMSAP1 and FAM134B. Of these, the RAB18-SPG20 interaction was previously validated (Gillingham et al., 2014), BICD2 interacts with RAB18 among a number of Rab isoforms (Gillingham et al., 2019, Gillingham et al., 2014) and REEP4 was previously shown to interact with RAB3GAP (Tinti et al., 2012). Although not previously linked to RAB18, CAMSAP1 and FAM134B were each identified in both HEK293 and HeLa datasets. Next, a group of proteins involved in establishing membrane contacts included components of the NRZ/Dsl1 membrane-tethering complex, ZW10, RINT1 and NBAS, the Sec1/Munc18 (SM) protein SCFD2 and SNAP-REceptor (SNARE) proteins STX18 and BNIP1.

These proteins have been previously studied in the context of RAB18 (Gillingham et al., 2019, Gillingham et al., 2014, Li et al., 2019, Xu et al., 2018, Zhao & Imperiale, 2017). Also in this group were the SNARE protein homologue SEC22A and the ER-resident multispanning transmembrane protein WFS1, which regulates membrane contacts between the ER and mitochondria (Angebault et al., 2018). These latter proteins had not been linked to RAB18 previously. The third group of proteins associated with RAB18 were a number of lipid transport, exchange and modifying proteins, C2CD2L, C2CD2, ORP2/OSBPL2, INPP5B, EBP and TMCO4. Interestingly, all but TMCO4 have related lipid species as their known substrates. C2CD2 and C2CD2L are thought to mediate phosphatidylinositol (PI) transfer between apposed membranes (Lees et al., 2017), ORP2 has recently been shown to exchange PI(4,5)P_2 and cholesterol and INPP5B hydrolyses PI(4,5)P_2 to PI(4)P (Wang et al., 2019). EBP is a Δ8-Δ7 Sterol Isomerase involved in cholesterol biosynthesis (Silve et al., 1996). Various members of the OSBP family interact with Rab proteins (Gillingham et al., 2019, Johansson et al., 2005), and a number of Rab isoforms interact with INPP5B (Fukuda et al., 2008, Williams et al., 2007), though associations with RAB18 have not been previously reported.

For initial validation of our HeLa dataset, we first carried out an additional independent BioID experiment with wild-type and RAB3GAP1-null cells and subjected the resulting samples to Western blotting for selected RAB18-associated proteins (Figure 3A). As with the mass spectrometry, these proteins showed either complete (RAB3GAP1, RAB3GAP2, ZW10) or partial (SPG20, STX18) dependence on RAB3GAP for their RAB18 association.

Since RAB18 and its regulators are linked to Warburg Micro syndrome, we asked whether the putative RAB18 effectors were linked to any diseases with overlapping clinical features (Figure 3B). Micro syndrome is a clinically distinctive disorder characterised by intellectual disability (ID), postnatal microcephaly, brain malformations, ascending spastic paraplegia, neuropathy, hypogonadism and eye abnormalities that include congenital bilateral cataracts, microphthalmia, microcornea and optic atrophy (Handley & Sheridan, 2018). Among the RAB3GAP-dependent RAB18 associations identified in the BioID screen, we noted that several are encoded by disease-associated genes or their homologues. In common with Micro syndrome, diseases linked to *SPG20*, *BICD2*, and the *REEP4*-homologues

REEP1 and *REEP2* are associated with ascending paraplegia (hereditary spastic paraplegia/HSP). *FAM134B* is associated with sensory and autonomic neuropathy, while the eye features of Micro syndrome overlap a different set of genes. *EBP* is linked to microphthalmia, microcornea and cataracts as well as to brain malformations like those in Micro syndrome. Both *WFS1* and *NBAS* have been linked to conditions associated with optic atrophy, and both *WFS1* and the INPP5B homologues OCRL1 and INPP5K are linked to conditions associated with congenital cataracts.

Given the suggestive convergences in protein function and gene-disease-associations, we proceeded to examine the subcellular localizations of 12 putative effectors for which antibodies were available (Figure 3C-D). To determine whether the localization of these proteins was altered in cells lacking RAB18, we analysed wild type and RAB18-null lines in each case. In order to directly compare cells of different genotypes under otherwise identical conditions, we labelled them with CellTrace-Violet and CellTrace-Far Red reagents before seeding, immunostaining and imaging them together. Since RAB18 can localize to LDs, we analysed both untreated cells (Figure 3C) and cells loaded with oleic acid and labelled with BODIPY-558/568-C12 (Figure 3D).

We observed a variety of staining patterns for the different putative effector proteins. These ranged from staining that was enriched at the perinuclear region of cells, to staining that appeared reticular, to staining that appeared more diffuse (Figure 3C). Each staining pattern was compatible with the known localization of RAB18, which is distributed between *cis*-Golgi, ER and cytosolic compartments (Handley et al., 2015). Staining patterns for individual proteins were similar in the HeLa cells and also in wild-type and RAB18-null RPE1 cells generated to provide biological replicates (Figure S5). In lipid-loaded cells, we observed that the localizations of proteins with reticular staining patterns overlapped with LDs, but they did not obviously shift to adopt an LD localization. However, the two proteins that showed the most diffuse staining patterns in untreated cells - ZW10 and SPG20 - appeared enriched in the vicinity of LDs in lipid-loaded cells (Figure 3D).

We saw no evidence for dramatic changes in protein localizations in RAB18-null cells as compared to their wild-type counterparts. Fluorescence intensities in RAB18-null and wild-type cells were also generally similar, except in the case of staining for

SPG20, in which it appeared lower in RAB18-null HeLa cells than in wild-type cells (Figure 3C).

Levels of SPG20 are significantly reduced in RAB18-null and TBC1D20-null cells

In a RAB18-null mouse model of Warburg Micro syndrome, peripheral nerves have a disordered cytoskeleton, and there is a striking accumulation of microtubules at motor nerve terminals (Carpanini et al., 2014). Therefore, interactions between RAB18 and microtubule-binding proteins is of particular interest. To confirm the reduction in levels of SPG20 we observed in RAB18-null HeLa cells, we used quantitative fluorescence microscopy (Figure 4A-C). The SPG20 antibody used in this study has previously been used for this purpose (Nicholson et al., 2015). However, to confirm its specificity and also to determine the levels of non-specific background produced in our experiments, we first analysed SPG20-null cells (Figure 4A-B). Measured fluorescence intensity of SPG20-null cells provided a baseline level, above which fluorescence levels are proportional to levels of SPG20. In RAB18-null cells, SPG20 fluorescence was reduced to 67.16±3.77% (s.e.m., $p<0.001$) of that in wild-type cells (Figure 4C).

To determine whether levels of SPG20 were altered by disrupted RAB18 regulation, we next compared SPG20 fluorescence of wild type, RAB3GAP1-, RAB3GAP2- and TBC1D20-null cells. Loss of the RAB18-GEF subunits RAB3GAP1 or RAB3GAP2 did not significantly affect levels of SPG20, whereas loss of the RAB18-GAP TBC1D20 led to a reduction comparable to that in RAB18-null cells (57.48%±2.57 (s.e.m., $p<0.00005$). To rule-out the possibility that reduced SPG20 levels in RAB18- and TBC1D20-null HeLa cells were the result of clonal variation, we analysed the corresponding panel of RPE1 cell lines. However, because the RPE1 cells were less amenable to comparative immunofluorescence experiments than HeLa cells, we used LFQ analysis of whole cell lysates. As in the HeLa cells, levels of SPG20 were significantly reduced in RAB18- and TBC1D20-null RPE1 cells compared to wild-type controls ($p<0.05$ following FDR correction), but not in the other genotypes tested (Figure 4D, Table S3).

RAB18, TBC1D20 and the RAB3GAP complex have all been linked to roles in proteostasis and autophagy (Bekbulat et al., 2018, Feldmann et al., 2017, Sidjanin et

al., 2016, Spang et al., 2014). It was therefore possible that reduced SPG20 levels in RAB18- and TBC1D20-null cells were the result of widespread dysregulation of proteostasis. To assess this possibility, we compared LFQ data from wild-type and TBC1D20-null RPE1 and HeLa cells (Tables S3 and S4). Following FDR correction, only a small number of proteins showed significantly altered levels in each cell type and there was limited overlap between cell types. This is in-line with a recent study showing a compensatory mechanism maintains levels of basal autophagy when RAB18 is absent or dysregulated (Bekbulat et al., 2018). Thus, dysregulation of SPG20 levels most likely arises from a discrete mechanism.

Discrete changes in SPG20 levels in RAB18- and TBC1D20-null cells together with the previous report of a RAB18-SPG20 interaction (Gillingham et al., 2014) provided strong evidence for a functional relationship between these proteins. We therefore carried out co-expression experiments to determine whether they colocalize in cells. Coexpression of mCherry-RAB18 and mEmerald-SPG20 in HeLa cells showed that, as previously reported, mCherry-RAB18 adopts a largely reticular localization (Gerondopoulos et al., 2014) whereas mEmerald-SPG20 appears largely diffuse (Eastman et al., 2009)(Figure 4E). We did not observe any clear colocalization between the proteins or any relocalization of mEmerald-SPG20 in cells expressing mCherry-RAB18. Since both RAB18 and SPG20 localize to LDs, we next explored whether the localization of either protein to LDs was dependent on the other. In oleic acid/BODIPY-558/568-C12-loaded HeLa cells, we found that mEmerald-SPG20 became concentrated around LDs, but that its localization was similar in both wild-type and RAB18-null cells (Figure 4F, left panels). Similarly, EGFP-RAB18 was enriched around LDs in both wild-type and SPG20-null cells (Figure 4F, right panels).

Collectively, our findings suggest that RAB18 and SPG20 become localized to LDs independently, and that any RAB18-SPG20 interaction is likely to be transient. The reduced levels of SPG20 in RAB18- and TBC1D20-null cells seem likely to result from its reduced stability, and it is intriguing that a transient interaction could influence this. Nevertheless, this is consistent with the involvement of TBC1D20-catalysed RAB18 GTP-hydrolysis and accompanying conformational change.

SEC22A associates with RAB18 and its knockdown causes altered LD morphology

The most studied group of RAB18 effector proteins to date are the tethering factors ZW10, NBAS and RINT1, which together comprise the NRZ/Dsl1 complex (Gillingham et al., 2014, Li et al., 2019, Xu et al., 2018, Zhao & Imperiale, 2017). The NRZ complex regulates assembly of an ER SNARE complex containing STX18. The canonical, fusogenic, form of this complex contains STX18, BNIP1, USE1 and SEC22B (Spang, 2012, Tagaya et al., 2014). However, it has been proposed that SEC22B is dispensable for the functions of RAB18, the NRZ complex, STX18, BNIP1 and USE1 in regulating LDs (Xu et al., 2018). Rather than promoting membrane fusion it is suggested that, in the absence of SEC22B, these proteins can mediate the close apposition of membranes to facilitate lipid transfer.

In the HEK293 and HeLa BioID datasets, RAB18-associations with all three NRZ components were nucleotide-binding-dependent and RAB3GAP-dependent respectively (Figures 1B, 2D, Tables S1, S2). In the HeLa dataset, the ER SNARE proteins STX18 and BNIP1 were also identified as associating with RAB18 in a RAB3GAP-dependent manner (Figure 2D, Table S2). Interestingly, also among the RAB3GAP-dependent RAB18 associations was SEC22A, a poorly studied homologue of SEC22B.

SEC22A is one of two SEC22B homologues in humans, the other being SEC22C. Like SEC22B, SEC22A and SEC22C possess N-terminal Longin domains and C-terminal transmembrane (TM) domains. However, they lack the central coiled-coil SNARE domain through which SEC22B mediates membrane fusion as part of the STX18 complex. SEC22B localizes to the ER–Golgi intermediate compartment, whereas different isoforms of SEC22C localize to the ER or *cis*-Golgi (Ge et al., 2013, Yamamoto et al., 2017, Zhang et al., 1999). The localization of SEC22A had not been addressed. In the absence of commercially available antibodies for SEC22A, we examined its localization through expression of an mEmerald-SEC22A fusion protein (Figure 5A). mEmerald-SEC22A produced a characteristic reticular staining pattern and colocalized with an exogenous ER marker suggesting that SEC22A localizes to the ER.

We next sought to compare the localization of SEC22A and RAB18 and to determine whether they interact. However, coexpression of mEmerald-SEC22A and mCherry-

RAB18 appeared to disrupt normal ER morphology and to produce vesicular structures and inclusions positive for both proteins (Figure S6). Although this was not inconsistent with a protein-protein interaction, it precluded the use of coexpressed exogenous proteins to test such an interaction. We therefore used a BirA*-SEC22A fusion protein to verify the RAB18-SEC22A association, to identify other SEC22A-associations, and to determine whether these associations were influenced by the absence of RAB18 or its regulators. To minimize potential toxicity while increasing biotin-ligase activity, we used BioID2 (Kim et al., 2016) with a p.Gly40Ser active site modification (Branon et al., 2018) and reduced biotin incubation time to 6 hours. LFQ analysis following streptavidin pull-down and mass spectrometry indicated that BioID2(Gly40S)-SEC22A was present at much lower levels than the BirA*-RAB18 in the prior experiments (3.79±0.96%). However, after adjusting for non-specific binding and normalizing the data according to the quantity of BioID2(Gly40S)-SEC22A in each sample, the construct appeared to label RAB18 in a RAB3GAP-dependent manner (Figure 5B). RAB3GAP1 and RAB3GAP2, as well as the putative RAB18-associated proteins REEP4 and BICD2, were among 55 SEC22A-associated proteins present in samples from wild-type cells in >2 replicate experiments and represented by >3 spectral counts (Table S5). Furthermore, also among these proteins, a subset of 9 SEC22A-associations were attenuated (association ratios <0.5) in samples from both RAB18-null and RAB3GAP-null cells. Broadly, these data were consistent with a functional SEC22A-RAB18 interaction.

Given the involvement of RAB18, the NRZ complex, and a STX18 complex lacking SEC22B in the regulation of LDs, we asked whether SEC22A might also be involved. Multiple studies have shown that LD morphology is altered in lipid-loaded cells in which RAB18 expression - or that of its regulators - is disrupted or silenced, with fewer and/or larger LDs are observed in these cells compared to controls (Bekbulat et al., 2018, Carpanini et al., 2014, Gerondopoulos et al., 2014, Li et al., 2017, Liegel et al., 2013, Xu et al., 2018). Similar observations have been made in ZW10-, NBAS-, STX18-, BNIP1- and USE1-null cells, whereas LD size distribution is unaltered when SEC22B expression is silenced (Xu et al., 2018). We examined the effects of silencing ZW10, NBAS and SEC22A in oleic acid-loaded immortalized human hepatocyte (IHH) cells (Figure 5C). ZW10 and NBAS silencing provided positive controls.

ZW10 silencing led to a significant reduction in LD number ($p<0.001$) compared to controls, whereas NBAS silencing led to both a significant reduction in LD number and a significant increase in LD size ($p<0.001$ in each case). The effects of SEC22A silencing mirrored those of NBAS silencing, producing a significant reduction in LD number ($p<0.001$) and a significant increase in LD size ($p<0.001$). Together, these data implicate SEC22A in RAB18-mediated LD regulation.

RAB18 recruits the orphan lipase TMCO4 to the ER membrane in a RAB3GAP-dependent manner

Among the lipid modifying/mobilizing proteins identified as potential RAB18 effectors in HeLa cells, TMCO4 was identified in all three replicate experiments and its association with RAB18 was highly RAB3GAP-dependent (association ratio 0.06). TMCO4 (transmembrane and coiled-coil domains 4) is annotated as containing transmembrane and coiled-coil domains, but is orthologous to the Yeast protein Mil1/ Yfl034w. Mil1 was found to be peripherally membrane-associated/soluble, and is thought to be an α/β hydrolase and a probable lipase based on structural modelling (Whitfield et al., 2016). Consistent with this, a catalytic triad within its predicted active site was shown to be required to confer tolerance to the membrane-intercalating cationic amphipathic drug sertraline (Whitfield et al., 2016). The best template match produced for TMCO4 by the structural modelling tool Phyre2 (Kelley et al., 2015) is an acylglycerol/diacyclglycerol lipase (Figure S7). To explore the localization of TMCO4, we expressed TMCO4-EGFP in HeLa cells (Figure 6A). This construct showed a diffuse appearance consistent with a largely cytosolic localization. In contrast, EGFP-RAB18 partly localizes to the ER, as shown by its colocalization with an ER marker.

To assess the potential interaction between RAB18 and TMCO4, we coexpressed mCherry-RAB18 and TMCO4-EGFP (Figure 6B). As in our previous experiments, we used Celltrace reagents to distinguish cells of wild-type and mutant genotypes and imaged these on the same dishes. In wild-type HeLa cells, we found that the coexpression of mCherry-RAB18 led to a dramatic redistribution of TMCO4-EGFP to the ER membrane suggesting that RAB18 is involved in the recruitment of TMCO4 to this compartment (Figure 6B, upper panels). This redistribution was completely

absent in RAB3GAP1- and RAB3GAP2-null cells but unaffected in TRAPPC9-null cells consistent with the BioID data. As a means of verifying the interaction, we carried out immunoprecipitation experiments using exogenous HA-RAB18 and TMCO4-EGFP (Figure 6C). As expected, TMCO4-EGFP copurified with HA-RAB18 when expressed in wild-type or TRAPPC9-null cells, but not when expressed in RAB3GAP1-null cells. These data indicate that RAB18 and TMCO4 interact directly or indirectly as part of a protein complex in a RAB3GAP-dependent manner. Further, both the microscopy and the immunoprecipitation data support the suggestion that different GEFs can promote different RAB18-interactions.

RAB18 is involved in cholesterol mobilization and biosynthesis

The lipid-related RAB3GAP-dependent RAB18-associated proteins in the HeLa BioID dataset included ORP2/OSBPL2 and INPP5B, which are robustly linked to a role in cholesterol mobilization. ORP2 is thought to function as a lipid transfer protein that delivers cholesterol to the plasma membrane (PM) in exchange for PI(4,5)P_2, whereas INPP5B is implicated in the hydrolysis of ORP2-bound PI(4,5)P_2, presumably driving the exchange process (Wang et al., 2019). Two other proteins in this group, C2CD2L/TMEM24 and C2CD2, have not been linked to cholesterol, but C2CD2L is characterised as a PI transporter and found to promote PM PI(4,5)P_2 production (Lees et al., 2017). On the basis of these findings, we investigated the potential role of RAB18 in cholesterol uptake and efflux.

We performed loading and efflux experiments to demonstrate the flux of cholesterol/cholesteryl ester (CE) based on the activity of RAB18. Chinese hamster ovary (CHO) cells were generated to stably express RAB18(WT), RAB18(Gln67Leu), or RAB18(Ser22Asn)(Figure S8). These cells were then preincubated with lipoprotein deficient serum (LPDS) before addition of [^{14}C]-oleate for 24 hours. [^{14}C]-oleate was added in the presence of LPDS (Figure 7A, left panel) or 10% FBS (Figure 7A, right panel). [^{14}C]-CE levels were measured at t=0, and efflux was assessed by measuring CE levels 4 and 8 hours following the addition of high density lipoprotein (HDL) to the cells. In each case, [^{14}C]-CE was isolated by thin layer chromatography (TLC) and quantified by scintillation counting. Efflux was also assessed directly by loading the cells with [^{3}H]-cholesterol, then incubating them with

apolipoprotein (apo) A-I. [^{3}H]-cholesterol associated with apoA-I in the medium, as a percentage of total cellular radioactivity, is shown in Figure 7B.

In cells loaded with [^{14}C]-oleate/LPDS, levels of CE were comparable in RAB18(Ser22Asn) and RAB18(WT) cells, whereas RAB18(Gln67Leu) cells stored significantly more (Figure 7A, left panel). In cells loaded with [^{14}C]-oleate/FBS, levels of CE in RAB18(Ser22Asn) remained unchanged, whereas its storage was elevated in RAB18(WT) cells and RAB18(Gln67Leu) cells (Figure 7A, right panel). Interestingly, in both [^{14}C]-oleate/LPDS-loaded and [^{14}C]-oleate/FBS-loaded cells, the addition of HDL led to rapid depletion of CE in RAB18(Gln67Leu) cells, but not in RAB18(Ser22Asn) or RAB18(WT) cells (Figure 7A). Consistently, [^{3}H]-cholesterol also underwent significantly more rapid efflux from these cells (Figure 7B).

The above data indicated that 'activated' GTP-bound RAB18 strongly promotes the turnover and mobilization of CE and were consistent with a role for RAB18 in mediating cholesterol mobilization via ORP2. Given that RAB18 also associated with EBP in our HeLa dataset, we next explored whether RAB18 might be necessary for the mobilization of substrates or products of EBP-catalysis. EBP is involved in *de novo* cholesterol biosynthesis (Silve et al., 1996). In the Bloch pathway, it catalyses the conversion of 5α-cholesta-8, 24-dien-3β-ol (zymosterol) to 5α-cholesta-7, 24-dien-3β-ol (24-dehydrolathosterol). In the Kandutsch-Russel pathway, it catalyses the conversion of 5α-cholest-8(9)-en-3β-ol (zymostenol) to 5α-cholest-7-en-3β-ol (lathosterol)(Platt et al., 2014). To identify any alteration in sterol levels in RAB18-null HeLa cells as compared to wild-type cells, we first incubated them for 48 hours in media supplemented with LPDS, then subjected samples to analysis by GC-MS (Figure 7C).

In RAB18-null cells, we found that levels of the EBP substrate zymostenol were not significantly different from those in wild-type cells. In contrast, levels of its product lathosterol were significantly increased ($p<0.01$). These data are consistent with intracellular accumulation of lathosterol resulting from a failure in its mobilization away from the site of its generation by EBP (Figure 7D). Levels of the downstream intermediate desmosterol were significantly reduced in RAB18-null ($p<0.01$), consistent with impaired delivery of substrates to post-EBP biosynthetic enzymes.

We reasoned that impaired delivery of cholesterol precursors to post-EBP enzymes might reduce cholesterol biosynthesis in cells in which RAB18 is absent or dysregulated. We therefore assessed cholesterol biosynthesis in the HeLa cell lines by incubating them for 24 hours in media supplemented with LPDS, then treating them for 24 hours with [^{3}H]-acetate or [^{3}H]-mevalonate (Figure 7E-F). Free cholesterol was separated by TLC and labelled cholesterol was quantified by scintillation counting. Under both conditions, labelling was similar in two clonal wild-type cell lines, but was reduced in RAB18-, RAB3GAP1-, RAB3GAP2-, TBC1D20- and TRAPPC9-null cells. Labelling was lowest in RAB18-null cells (6.8±0.5% of wild-type controls for acetate, 39.5±2.5% for mevalonate) and slightly higher in the RAB3GAP1-, RAB3GAP2-, TBC1D20- and TRAPPC9-null lines (23±2%-43±3% for acetate, 46±2.5%-73±5% for mevalonate). These data strongly suggest that RAB18 and its regulators are required for normal cholesterol biosynthesis.

Our model for the involvement of RAB18 in cholesterol biosynthesis is that it is facilitates mobilization of EBP-products including lathosterol via ORP2 (Figure 7D). Structural data are available for the ORP2 OSBP-related domain (ORD)(Wang et al., 2019). Therefore, to test our model, we generated molecular dynamics simulations of the ORP2-ORD incorporating either cholesterol or lathosterol (Figure 7G-H, Figure S9, Videos S1-S2). Over 300ns, both simulations remained comparably stable in terms of positional root-mean-square deviation (RSMD)(Figure S9A). The pattern of positional root mean square fluctuations (RSMFs) for ORP2-ORD amino acid residues in each simulation was also largely similar although some differences were evident (Figure S9B). Among residues in the vicinity of the sterol, only a single Tyr residue (Tyr110 in NP_653081) showed a clear difference. This residue appeared to fluctuate less in the presence of lathosterol than in the presence of cholesterol.

Examination of the simulations suggested that Tyr110 adopts different positions in the presence of the different sterols (Figure 7G-H, Figure S9C, Videos S1-S2). The 3-hydroxyl of cholesterol maintains a relatively stable distance from the Tyr. In contrast, the 3-hydroxyl of lathosterol is frequently closer to the Tyr-hydroxyl, though this varies over the timecourse (Figure S9C). In crystal structures of the OSBP-related protein Osh4 and sterols, it was noted that water-mediated interactions were prominent (Im et al., 2005). Therefore, we explored the positioning of water molecules with respect to lathosterol and cholesterol in our simulations. Interestingly,

water molecules were much more frequently found in close proximity to the lathosterol 3-hydroxyl than to the cholesterol 3-hydroxyl (Figure S9D). Together, these data suggest that the ligand-binding tunnel of ORP2 adopts a relatively stable but distinct conformations when bound to cholesterol or lathosterol. Despite their minor structural differences, stabilization of the lathosterol 3-hydroxyl appears to involve water-mediated interactions to a greater degree than that of the cholesterol 3-hydroxyl. Plots of the RMSFs of the atoms in each sterol (Figure S9E) show generally higher fluctuations with lathosterol than with cholesterol. Speculatively, this may suggest that the interaction with lathosterol is entropically more favourable.

DISCUSSION

The data presented in this study provide preliminary evidence that Warburg Micro syndrome/RAB18 deficiency is associated with disrupted *de novo* cholesterol biosynthesis. We have shown that lathosterol accumulates in RAB18-null HeLa cells suggesting that its delivery to lathosterol oxidase (SC5DL) is impaired. Further, we have shown that levels of cholesterol biosynthesis are reduced when RAB18 or its regulators are absent. Pathogenic variants in *SC5DL* cause the rare recessive disease lathosterolosis, which shares overlapping features with Micro syndrome including microcephaly, intellectual disability, micrognathia, high arched palate and cataract (Anderson et al., 2019, Brunetti-Pierri et al., 2002, Ho et al., 2014, Krakowiak et al., 2003, Rossi et al., 2007). Similarly, the next enzyme in the pathway is encoded by *DHCR7*, in which pathogenic variants cause Smith-Lemli-Opitz syndrome (SLOS)(Nowaczyk & Wassif, 1998). While the symptoms of this disorder can be highly variable, it is among the top differential diagnoses for Micro syndrome (Handley & Sheridan, 2018).

Confirmation that features of Micro syndrome pathology arise from impaired cholesterol biosynthesis could spur development of therapeutic strategies to treat the disease. In SLOS, cholesterol supplementation has been widely used and more recently is being combined with antioxidants with the aim of reducing toxicity from aberrant cholesterol metabolites (Fliesler et al., 2018, Korade et al., 2014, Svoboda et al., 2012). Supplementation with fat soluble vitamins may balance deficiencies. Finally, paradoxical treatment with certain statins has been used in both SLOS and lathosterolosis and may increase the expression of DHCR7 (Correa-Cerro et al., 2006, Ho et al., 2014, Wassif et al., 2017). Careful clinical research will be required to determine whether such interventions are safe, and whether they have any efficacy in Micro syndrome.

In this study, we have complemented previous work showing that proximity biotinylation is a powerful means of identifying candidate Rab effectors (Gillingham et al., 2019). Further – at least in the case of RAB18 - we have found that comparing biotin-labelling produced by a BirA*-Rab in wild-type and GEF-deficient cells can be particularly informative. We found that marked reductions in RAB18-association in RAB3GAP-null cells were restricted to a relatively small number of proteins and that these comprised known and/or plausible interactors. By identifying these, we were

able to exclude ~95% of RAB18-associations from consideration as more likely to represent 'noise' from bystander proteins. Interestingly, we found that the disruption of different GEF complexes affected largely distinct subsets of RAB18 associations. This may indicate that different RAB18-GEFs control different aspects of RAB18 function.

It has been proposed that RAB18 functions to coordinate lipid transfer between apposed membranes, and our RAB3GAP-dependent interaction data are consistent with this model (Xu et al., 2018). The 25 RAB3GAP-dependent RAB18 interactors we identified include microtubule-interacting/membrane-remodelling proteins, proteins involved in bringing membranes into close apposition, and proteins involved in lipid modification and mobilization. It seems likely that membrane remodelling precedes the engagement of tethers and SNAREs and the establishment of membrane-contacts. Lipid transporter/exchange proteins are required for lipid transfer to occur at these contact points, while lipid-modifying proteins may serve to generate substrates for transport and/or concentration gradients necessary to promote this transport.

Three key RAB18 interactors identified in our study were ORP2, INPP5B and EBP. ORP2 is thought to act as sterol-PI(4,5)P_2 exchanger, whereas INPP5B is thought to drive the exchange process by catalysing PI(4,5)P_2 hydrolysis (Wang et al., 2019). The finding that these proteins each associate with RAB18 may suggest that they function in an analogous manner to OSBP, the phosphatase SACM1L (SAC1) and the ARF1 GTPase in mediating sterol exchange (Antonny et al., 2018). Because of the role EBP in cholesterol biosynthesis, we were prompted to explore whether substrates or products of EBP-catalysis accumulated in the absence of RAB18. The finding that lathosterol but not zymostenol accumulates suggests that RAB18 is required to coordinate the mobilization of EBP-products via ORP2 (Figure 7E).

The potential role of the other lipid-related proteins identified in our screen, C2CD2L, C2CD2 and TMCO4, is less clear. However, since C2CD2L is found to transport PI and to promote PI(4,5)P_2 generation (Lees et al., 2017), it is possible it functions in concert with ORP2 and INPP5B. TMCO4 is poorly characterized. However, it was identified in one study as one of a number of genes with upregulated expression in rabbit cerebral arteries under conditions of hypercholesterolemia (Ong et al., 2013). Another study suggests it is present on lipid rafts (Jin et al., 2012).

The regulated transport of specific sterol intermediates by RAB18 raises the possibility that other Rab proteins might regulate transport of other intermediates or regulate the biosynthetic pathways of other lipid species. In addition, it is possible that particular intermediates might be delivered to different subcellular locations via different Rabs. Interestingly, INPP5B has been shown in several studies to have a broad Rab-binding specificity (Fukuda et al., 2008, Williams et al., 2007). Further, many other phosphoinositide phosphatase enzymes, including members from distinct protein families, bind to Rab proteins (Gillingham et al., 2019). Similarly, multiple OSBP-homologues also bind to Rabs (Gillingham et al., 2019, Rocha et al., 2009, Sobajima et al., 2018, Zhao & Ridgway, 2017). Thus, it is possible that different Rab isoforms may specify intermembrane transfer of different sterols by association with different combinations of phosphatase and OSBP proteins.

Differential mobilization of intermediates by discrete OSBP-INPP-Rab combinations is one possible explanation for prominent features of lathosterolosis and SLOS that do not overlap with Micro syndrome. Several such features resemble those caused by impaired ciliogenesis, ciliary function or Sonic Hedgehog (SHH) deficiency, and are ascribed to a deficit in cholesterol at the cilium (Blassberg et al., 2016, Nowaczyk & Wassif, 1998). It may be that cholesterol biosynthesis at, or its delivery to cilia, is less affected in Micro syndrome because alternative lipid transfer mechanisms are involved.

One of the clinical features present in Micro syndrome but not in lathosterolosis or SLOS is ascending spastic paraplegia. In this context, the reduced levels of SPG20 in RAB18- and TBC1D20-null cells may be relevant. Biallelic loss-of-function variants in *SPG20* cause Troyer syndrome, a complex HSP also characterized by ascending paraplegia (Baple & Crosby, 2004). SPG20 is a protein of enigmatic function, but one possible avenue for future research could be the potential relationship between SPG20 and the other RAB18-associated microtubule (MT)-binding proteins identified in this study. Like SPG20, CAMSAP1 is found to associate with poles of the mitotic spindle (Hueschen et al., 2017, Lind et al., 2011). CAMSAP1 is a MT minus-end binding protein whereas BICD2 is a component of a minus-end-directed dynein-dynactin motor complex (Hendershott & Vale, 2014, Hueschen et al., 2017, Urnavicius et al., 2015). REEP4 is localized to the ER, and like RAB18 is linked to the regulation of ER structure (Gerondopoulos et al., 2014, Kumar et al., 2019).

However, it also contributes to the clearance of ER from metaphase chromatin (Schlaitz et al., 2013). This role is dependent on its MT-binding, and therefore spindle-binding during metaphase. Thus, these four MT-binding proteins all appear to function in the same spatiotemporally defined compartment during mitosis (Figure S10A).

Among the membrane tethering and docking proteins associated with RAB18, we investigated SEC22A on the basis of its homology to SEC22B. SEC22B is a component of the canonical, fusogenic, syntaxin 18 SNARE complex. Other components of this complex interact with RAB18 to regulate membrane contacts, though SEC22B itself is not necessary for this activity (Xu et al., 2018). Reciprocal proximity biotinylation with a BioID2-SEC22A fusion was consistent with a RAB3GAP-dependent RAB18-SEC22A interaction, and suggested that other SEC22A interactions are altered when RAB18 is absent or dysregulated. We also found that the silencing of SEC22A led to altered LD morphology, similar to that previously observed when expression of other RAB18-associated tethering/docking proteins was disrupted. Though our data are tentative, it is tempting to speculate that SEC22A contributes to a non-fusogenic SNARE complex, since it lacks the SNARE domain usually required to provide the mechanical force for fusion (Figure S10B). SNARE proteins can be relatively promiscuous in their interactions, and there are numerous examples of individual SNAREs contributing to distinct SNARE complexes (Petkovic et al., 2014, Wang et al., 2017). There are also examples in which SNARE complexes mediate the stable association of membranes rather than their fusion (Petkovic et al., 2014).

To summarise, we have used complementary proximity ligation approaches together with CRISPR gene-editing to inventory RAB18-associated proteins. The RAB3GAP-dependent RAB18-associations we have highlighted are supported by additional validation and functional evidence as well as by correlative information from the literature. Broadly, the latter suggests a role for Rab proteins distinct from that in mediating vesicular membrane traffic. Another role of Rabs may be to assemble a network of diverse membrane-membrane contact sites and then orchestrate highly regulated metabolism and flow of lipid species within a discontinuous lipid phase. Disruption of specific contact sites can produce metabolic deficiency and may cause human disease.

MATERIALS AND METHODS

Plasmids

Generation of recombinant pcDNA5 FRT/TO FLAG-BirA(Arg118Gly) vectors for preparation of stable T-Rex-293 cell lines is described below. Generation of recombinant pX461 and pX462 plasmids for CRISPR gene-editing is described below. Generation of recombinant pCMV vectors for preparation of stable CHO cell lines is described below. The EGFP-RAB18 construct has been described previously (Gerondopoulos et al., 2014). The RAB18 sequence was excised from this construct using BamHI and HindIII restriction enzymes (New England Biolabs, Hitchin, UK), and used to generate constructs encoding mEmerald-RAB18 and mCherry-RAB18 by ligation into mEmerald-C1 and mCherry-C1 vectors (Addgene, Watertown, MA) using HC T4 Ligase and rapid ligation buffer (Promega, Southampton, UK). Constructs encoding BirA*-RAB18, BioID2(Gly40Ser)-SEC22A, mEmerald-SEC22A, mEmerald-SPG20 and mEmerald-RAB7A were generated following PCR amplification from template and subcloning into an intermediate pCR-Blunt II-TOPO vector using a Zero Blunt TOPO PCR Cloning Kit (ThermoFisher Scientific, Waltham, MA) according to manufacturer's instructions. Fragments were excised from intermediate vectors and then subcloned into target vectors using restriction-ligation, as above. A construct encoding mCherry-ER was obtained from Addgene, and a construct encoding TMCO4-EGFP was synthesised and cloned by GeneWiz (Leipzig, Germany). Details of PCR templates, primers and target vectors are listed in Table S6.

Antibodies and reagents

A custom polyclonal antibody to RAB18 generated by Eurogentec (Southampton, UK) has been described previously (Handley et al., 2015). An antibody to RAB3GAP1 was obtained from Bethyl Labs (Montgomery, TX), an antibody to GFP was obtained from Takara Bio (Saint-Germain-en-Laye, France), an antibody to β-Tubulin was obtained from Abcam (Cambridge, UK) and an antibody to β-Actin was obtained from ThermoFisher. Antibodies to hemagglutinin (HA), RAB3GAP2 and TBC1D20 were obtained from Merck (Gillingham, UK). Antibodies to ZW10, STX18,

798 SPG20, RINT1, REEP4, BNIP1, C2CD2, TRIM13, WFS1, INPP5B, OSBPL2 and
799 NBAS were obtained from Proteintech (Manchester, UK). Antibody catalogue
800 numbers and the dilutions used in this study are listed in Table S6.

801

802 Cell culture

803 T-REx-293,HeLa and IHH cells were maintained in DMEM media, RPE1 cells in
804 DMEM/F12 media and CHO cells in alpha-MEM media (ThermoFisher). In each
805 case, media was supplemented with 10% foetal calf serum (FCS) and 1% penicillin-
806 streptomycin (PS). Cells were maintained at 37°C and 5% CO_2.

807

808 Generation of stable T-Rex-293 and CHO cell lines

809 PCR products encoding mouse RAB18, RAB18(Gln67Leu) and RAB18(Ser22Asn)
810 were subcloned into NotI-linearized pcDNA5 FRT/TO FLAG-BirA(Arg118Gly) vector
811 using the In-Fusion HD EcoDry Cloning Plus kit (Takara Bio) according to
812 manufacturer's instructions. Details of PCR templates, primers and target vectors are
813 listed in Table S6. 1.5ug of each recombinant vector together with 13.5ug of pOG44
814 plasmid (ThermoFisher) were used in cotransfections of T-REx-293 cells, in 10cm
815 dishes, with TransIT-LT1 Transfection Reagent (Mirus Bio, Madison, WI).16 hours
816 following transfection, media was replaced and cells were allowed to recover for 24
817 hours. Each dish was then split to 4x 10cm dishes in selection media containing 10
818 ug/ml Blasticidin and 50 ug/ml Hygromycin B. Resistant clones were pooled and
819 passaged once prior to use.

820 A PCR product encoding mouse RAB18 was subcloned into an intermediate TOPO
821 vector using a TOPO PCR Cloning Kit (ThermoFisher) according to manufacturer's
822 instructions. The RAB18 fragment was then excised and subcloned into the pCMV
823 vector. PCR-based site-directed mutagenesis using a GeneArt kit (ThermoFisher)
824 was then used to generate pCMV-RAB18(Gln67Leu) and pCMV-RAB18(Ser22Asn)
825 constructs. CHO cells were transfected using Lipofectamine 2000 reagent
826 (ThermoFisher) and cells stably-expressing each construct were selected-for with
827 blasticidin. Under continued selection, clonal cell-lines were grown from single cells
828 and then RAB18 protein expression was assessed. Cell lines comparably expressing

RAB18 constructs at levels 2.5-5x higher than those wild-type cells were used in subsequent experiments.

Generation of clonal 'knockout' HeLa and RPE1 cell lines

CRISPR/Cas9 gene-editing was carried out essentially as described in Ran et al., 2013 (Ran et al., 2013). Guide RNA (gRNA) sequences are shown in (Table S6). A list of the clonal cell lines generated for this study, together with the loss-of-function variants they carry is shown in (Figure S2A). Western blot validation is shown in (Figure S2B-E). Briefly, for each targeted exon, pairs of gRNA sequences were selected using the online CRISPR design tool (http://crispr.mit.edu/). Oligonucleotide pairs incorporating these sequences (Sigma) were annealed (at 50mM ea.) in 10mM Tris pH8, 50mM NaCl and 1mM EDTA by incubation at 95ºC for 10 minutes followed by cooling to room temperature. Annealed oligonucleotides were diluted and ligated into BbsI-digested pX461 and pX462 plasmids (Addgene) using HC T4 Ligase and rapid ligation buffer (Promega). Sequences of all recombinant plasmids were verified by direct sequencing. Pairs of plasmids were contransfected into cells using Lipofectamine 2000 reagent according to manufacturer's instructions. Cells were selected for puromycin resistance (conferred by pX462) using 24 hours puromycin-treatment. Following 12 hours recovery, they were selected for GFP fluorescence (conferred by pX461) and cloned using FACSAria2 SORP, Influx or FACSMelody instruments (BD, Wokingham, UK). After sufficient growth, clones were analysed by PCR of the targeted exons (Primers are listed in Table S6). In order to sequence individual gene edited-alleles, PCR products from each clone were first cloned into ZeroBlunt TOPO vector (ThermoFisher) and then subjected to colony PCR. These PCR products were then analysed by direct sequencing. Sequencing data was assessed using BioEdit software (http://www.mbio.ncsu.edu/BioEdit/bioedit.html).

BirA/BioID proximity labelling (T-REx-293 cells)

The T-REx-293 Cell Lines (described above) were seeded onto 3x 15cm plates each and allowed to adhere. Expression of BirA*-RAB18 fusion proteins was induced by treatment with 20ng/ml Tetracycline for 16 hours. Media was then replaced with media containing 20% FBS, 20 ng/ml Tetracycline and 50 uM Biotin and the cells

were incubated for a further 8 hours, washed with warmed PBS and pelleted in ice-cold PBS. Cell pellets were snap-frozen and stored at -80ºC prior to lysis. Lysis was carried out in 3ml of ice-cold RIPA buffer (150 mM NaCl, 1% NP40, 0.5% Sodium Deoxycholate, 0.1% SDS, 1mM EDTA, 50mM Tris, pH 7.4) supplemented with complete-mini protease inhibitor cocktail (Roche, Basel, Switzerland), 1mM PMSF, and 62.5 U/ml Benzonase (Merck). Lysates were incubated for 1 hour at 4ºC then sonicated in an ice bath (four 10 second bursts on low power). They were then clarified by centrifugation, and the supernatants transferred to tubes containing pre-washed streptavidin-sepharose (30µl bed-volume)(Merck). The beads were incubated for 3 hours at 4ºC, then washed x5 in RIPA buffer and x4 in buffer containing 100mM NaCl, 0.025% SDS and 25 mM Tris, pH7.4.

BirA*/BioID proximity labelling (HeLa cells)

Proximity-labelling in HeLa cells was carried out largely as described by Roux et al. (Roux et al., 2012), but with minor modifications. HeLa cells were grown to 80% confluence in T75 flasks and then each flask was transfected with 1-1.5µg of the BirA*-RAB18 construct or 1µg of the BioID2(Gly40Ser)-SEC22A construct using Lipofectamine 2000 reagent in Optimem serum-free medium (ThermoFisher) for 4 hours, according to manufacturer's instructions. 24 hours post-transfection, media was replaced with fresh media containing 50µM Biotin (Merck) and the cells were incubated for a further 24 or 6 hours (for BirA*-RAB18 and BioID2(Gly40Ser)-SEC22A experiments respectively). Cells were then trypsinised and washed twice in PBS before pellets were transferred to 2ml microcentrifuge tubes and snap-frozen. For each pellet, lysis was carried out in 420µl of a buffer containing 0.2% SDS, 6% Triton-X-100, 500mM NaCl, 1mM DTT, EDTA-free protease-inhibitor solution (Expedeon, Cambridge, UK), 50mM Tris pH7.4. Lysates were sonicated for 10 minutes using a Bioruptor device together with protein extraction beads (Diagenode, Denville, NJ). Each lysate was diluted with 1080µl 50mM Tris pH7.4, and they were then clarified by centrifugation at 20 000xg for 30 minutes at 4ºC. Affinity purification of biotinylated proteins was carried out by incubation of clarified lysates with streptavidin-coated magnetic Dynabeads (ThermoFisher) for 24 hours at 4ºC. Note that a mixture of Dynabeads - MyOne C1, MyOne T1, M270 and M280 – was used

to overcome a problem with bead-clumping observed when MyOne C1 beads were used alone. Successive washes were carried out at room temperature with 2% SDS, a buffer containing 1% Triton-X-100, 1mM EDTA, 500mM NaCl, 50mM HEPES pH7.5, a buffer containing 0.5% NP40, 1mM EDTA, 250mM LiCl, 10mM Tris pH7.4, 50mM Tris pH7.4 and 50mM ammonium bicarbonate.

Preparation of cell lysates for label-free quantitative proteomics

RPE1 and HeLa cells were grown to confluence in T75 flasks. They were then trypsinised, and cell pellets were washed with PBS and snap-frozen prior to use. RPE1 pellets were resuspended in 300µl 6M GnHCl, 75mM Tris, pH=8.5. HeLa pellets were resuspended in 300µl 8M urea, 75mM NaCl, 50mM Tris, pH=8.4. In each case, samples were sonicated for 10 minutes using a Bioruptor device together with protein extraction beads (Diagenode). RPE1 samples were heated for 5 minutes at 95ºC. Samples were clarified by centrifugation.

Mass spectrometry

Washed beads from BioID experiments with T-Rex-293 cell lines were resuspended in 50µl 6M urea, 2M thiourea, 10mM Tris, pH=8.5 and DTT was added to 1mM. After 30 minutes incubation at 37ºC, samples were alkylated with 5mM iodoacetamide (IAA) in the dark for 20minutes. DTT was increased to 5mM and 1µg lysC was added, then samples were incubated at 37ºC for 6 hours. Samples were diluted to 1.4M urea, then digested with trypsin (Promega), overnight at 37°C, according to manufacturer's instructions. Samples were acidified by the addition of 0.9% formic acid and 5% acetonitrile.

Washed beads from BioID experiments with HeLa cells were subjected to limited proteolysis by trypsin (0.3 ug) at 27°C for 6.5hours in 2mM urea, 1mM DTT, 75mM Tris, pH=8.5, then supernatants were incubated overnight at 37°C. Samples were alkylated with 50mM IAA in the dark for 20minutes, then acidified by addition of 8µl 10% trifluoroacetic acid (TFA). RPE1 lysates were reduced and alkylated through addition of tris(2-carboxyethyl)phosphine (TCEP) and 2-chloroacetamide (CAA) to 5mM and 10mM respectively and then incubated at 95°C for 5 minutes. After

924 cooling, samples were diluted to 3M guanidine and 0.5µg lysC added with incubation
925 overnight at 37°C. A further dilution to 1M guanidine was followed by digest with
926 0.3µg trypsin at 37°C for 4 hours. Samples were acidified with TFA. HeLa lysates
927 were reduced and alkylated by addition of DTT to 10mM, then by addition of IAA to
928 25mM, then further addition of DTT to 25mM, with incubation at room temperature
929 for 30-60 minutes following each step. Samples were digested with lysC, overnight at
930 37°C. They were then diluted to 2M urea, and further digested, overnight at 37°C.
931 Samples were acidified with TFA.

932 For BioID samples from T-REx-293 cells, LC-MS was carried out as previously
933 described (Brunet et al., 2016). Briefly, peptides in an aqueous solution containing
934 5% acetonitrile and 0.1% formic acid were loaded onto a 3 µm PepMap100, 2 cm, 75
935 µm diameter sample column using an Easy nLC 1000 ultrahigh pressure liquid
936 chromatography system (ThermoFisher). They were eluted with acetonitrile/formic
937 acid into an in-line 50 cm separating column (2 µm PepMap C18, 75 µm diameter) at
938 40°C. Separated peptides were ionized using an Easy Spray nano source and
939 subjected to MS/MS analysis using a Velos Orbitrap instrument (ThermoFisher).
940 Following acquisition, data were analysed using SEAQUEST software.

941 For other samples, peptides were loaded on to activated (methanol), equilibrated
942 (0.1% TFA) C18 stage tips before being washed with 0.1% TFA and eluted with
943 0.1% TFA/80 acetonitrile. The organic was dried off, 0.1% TFA added to 15 µl and 5
944 µl injected onto LC-MS. Peptides were separated on an Ultimate nano HPLC
945 instrument (ThermoFisher), and analysed on either an Orbitrap Lumos or a Q
946 Exactive Plus instrument (ThermoFisher). After data-dependent acquisition of HCD
947 fragmentation spectra, data were analysed using MaxQuant and the uniprot human
948 reference proteome. Versions, releases, parameters and gradients used for
949 separation are provided in table S6.

950

951 <u>Cell labelling</u>

952 In order to distinguish cells of different genotypes within the same well/on the same
953 coverslip, CellTrace Violet and CellTrace Far Red reagents (ThermoFisher) were
954 used to label cells before they were seeded. Cells of different genotypes were first
955 trypsinised and washed with PBS separately. They were then stained in suspension

by incubation with either 1µM CellTrace Violet or 200nM CellTrace Far Red for 20 minutes at 37°C. Remaining dye was removed by addition of a ten-fold excess of full media, incubation for a further 5 minutes, and then by centrifugation and resuspension of the resulting pellets in fresh media. Differently-labelled cells were combined prior to seeding.

Immunofluorescence microscopy

HeLa or RPE1 cells were seeded in 96-well glass-bottom plates (PerkinElmer, Waltham, MA) coated with Matrigel (Corning, Amsterdam, Netherlands) according to manufacturer's instructions, and allowed to adhere for 48 hours prior to fixation. In lipid-loading experiments, cells were treated with 200µM oleic acid complexed to albumin (Merck) and 1µg/ml BODIPY-558/568-C12 (ThermoFisher) for 15 hours prior to fixation. Cells were fixed using a solution of 3% deionised Glyoxal, 20% EtOH, 0.75% acetic acid, pH=5 (Richter et al., 2018), for 20 minutes at room temperature. They were then washed with PBS containing 0.9mM $CaCl_2$ and 0.5mM $MgCl_2$ and blocked with a sterile-filtered buffer containing 1% Milk, 2% donkey serum (Merck), 0.05% Triton-X-100 (Merck), 0.9mM $CaCl_2$ and 0.5mM $MgCl_2$ in PBS pH=7.4 for at least 1 hour prior to incubation with primary antibody. Primary antibodies were added in blocking buffer without Triton-X-100, and plates were incubated overnight at 4ºC. Antibody dilutions are listed in Table S6. Following washing in PBS, cells were incubated with 1:2000 Alexa 488-conjugated secondary antibody (ThermoFisher) in blocking buffer at room temperature for 1-2 hours. Following further washing in PBS, cells were imaged using an Operetta High Content Imaging System (PerkinElmer) equipped with Harmony software. In comparative fluorescence quantitation experiments, at least 18 frames – each containing >5 wild-type and >5 mutant cells – were analysed per genotype. ImageJ software was used to produce regions of interest (ROIs) corresponding to each cell using thresholding tools and images from the 405nm and 645nm channels. Median 490nm fluorescence intensity was measured for each cell and mutant fluorescence intensity (as %wild-type) was calculated for each frame and combined for each genotype.

Confocal microscopy – Live cell imaging

HeLa or RPE1 cells were seeded on glass-bottom dishes (World Precision Instruments, Hitchin, UK) coated with Matrigel (Corning) and allowed to adhere for 24 hours prior to transfection. Transfections and cotransfections were carried out with 0.5µg of each of the indicated constructs using Lipofectamine 2000 reagent in Optimem serum-free medium for 4 hours, according to manufacturer's instructions. Media were replaced and cells were allowed to recover for at least 18 hours prior to imaging. Imaging was carried out on a Nikon A1R confocal microscope equipped with the Nikon Perfect Focus System using a 60× oil immersion objective with a 1.4 numerical aperture. In immunofluorescence experiments, the pinhole was set to airy1. CellTrace Violet was excited using a 403.5nm laser, and emitted light was collected at 425–475nm. EGFP and mEmerald were excited using a 488 nm laser, and emitted light was collected at 500–550 nm. BODIPY-558/568-C12 and mCherry were excited using a 561.3 nm laser, and emitted light was collected at 570–620 nm. CellTrace Far Red was excited using a 638nm laser, and emitted light was collected at 663-738nm. In fluorescence recovery after photobleaching (FRAP) experiments, the pinhole was set to airy2 and digital zoom parameters were kept constant. Bleaching was carried out using 90% laser power.

Immunoprecipitation

HeLa cells were seeded onto 10cm dishes and allowed to adhere for 24 hours prior to transfection. Transfections and cotransfections were carried out with 0.5µg of each of the indicated constructs using Lipofectamine 2000 reagent in Optimem serum-free medium for 4 hours, according to manufacturer's instructions. 24 hours post-transfection cells were trypsinised, washed with PBS, then lysed in a buffer containing 150mM NaCl, 0.5% Triton-X-100 and EDTA-free protease-inhibitor solution (Expedeon), 10mM Tris, pH=7.4. Lysates were clarified by centrifugation, input samples taken, and the remaining supernatants then added to 4µg rabbit anti-HA antibody (Merck). After 30 minutes incubation at 4ºC on a rotator, 100µl washed protein G-coupled Dynabeads (ThermoFisher) were added and samples were incubated for a further 1 hour. The Dynabeads were washed x3 with buffer containing 150mM NaCl, 0.1% Triton-X-100, 10mM Tris, pH=7.4, then combined with a reducing loading buffer and subjected to SDS–PAGE.

Lipid loading experiments

For LD number and diameter measurements, IHH cells were seeded onto glass coverslips. siRNA transfections were carried out using FuGene reagent (Promega) according to manufacturer's instructions. siRNAs targeting ZW10 and NBAS were obtained from IDT, Coralville, IA; siRNA targeting SEC22A was obtained from Horizon Discovery, Cambridge, UK. 48 hours following transfection, cells were treated with 200nM BSA conjugated oleate for 24 hours. Coverslips were washed, fixed with 3% paraformaldehyde and stained with 1ug/mL BODIPY and 300nM DAPI. Fluorescence images were captured on a Zeiss LSM 780 confocal microscope equipped with a 100x objective. Images were analysed using ImageJ software. Data are derived from measurements from >100 cells/condition and are representative of three independent experiments.

For cholesterol storage and efflux experiments with [^{14}C]-oleate, CHO cell lines (described above) were seeded onto 12-well plates and then grown to 60-75% confluence in Alpha media supplemented with 10% LPDS. Cells were grown in the presence of 10% LPDS for at least 24 hours prior to the addition of oleate. 1 µCi/ml [^{14}C]-oleate (Perkin Elmer) was added in the presence of 10% LPDS or 10% FBS for 24 hours. Cells were then washed and incubated with 50µg/ml HDL for 0, 4 or 8 hours. Cellular lipids were extracted with hexane. Lipids were then dried-down and separated by thin layer chromatography (TLC) in a hexane:diethyl ether:acetic acid (80:20:2) solvent system. TLC plates were obtained from Analtech, Newark, NJ. Bands corresponding to cholesteryl ester (CE) were scraped from the TLC plate, and radioactivity was determined by scintillation counting in a Beckman Coulter LS6500 Scintillation Counter using BetaMax ES Liquid Scintillation Cocktail (ThermoFisher). Three independent experiments were carried out, each with four replicates of each condition. Data from a representative experiment are shown.

For cholesterol efflux experiments with [^{3}H]-cholesterol, CHO cells were seeded onto 12-well plates and then grown to 60% confluence in Alpha media supplemented with 10% FBS. 5 µCi/ml [^{3}H]-cholesterol (PerkinElmer) was added in the presence of 10% FBS. After 3x PBS washes, cells were incubated with serum-free media containing 25µg/ml of human apolipoprotein A-I (ApoA-I) for 5 hours. ApoA-I was a kind gift of Dr. Paul Weers (California State University, Long Beach). Radioactivity in aliquots of

media were determined by scintillation counting in a Beckman Coulter LS6500 Scintillation Counter using LSC Cocktail (PerkinElmer). Cell lysates were produced by addition of 0.1N NaOH for 1 hour, and their radioactivity was determined as above. Cholesterol efflux was calculated as an average (+/- SD) of the % cholesterol efflux (as a ratio of the media cpm/(media + cellular cpm) x 100%).

Sterol analysis

HeLa cells were grown to 80% confluence in T75 flasks, washed twice in PBS and then grown for a further 48 hours in DMEM supplemented with 10% LPDS. They were then trypsinised and washed twice in PBS before pellets were transferred to microcentrifuge tubes and snap-frozen. Pellets were resuspended in 200µl deionised water, sonicated for 20 seconds using an ultrasonic processor (Sonics & Materials Inc., CT, USA), then placed on ice. 750 µl of isopropanol containing 4 µmol/L 5α-cholestane as an internal standard was added to each sample, and then each was sonicated for a further 10 seconds. Lysates were transferred to 7ml glass vials and mixed with 250 µL tetramethylammonium hydroxide for alkalyine saponification at 80°C for 15 min, then cooled down for 10 minutes at room temperature. Sterols were extracted by addition of 500 µL tetrachloroethylene/methyl butyrate (1:3) and 2 ml deionised water, then thorough mixing. Samples were centrifuged for 10 minutes at 3000 rpm, and the organic phase containing the sterols was transferred to 300 µl GC vials. Extracts were dried under a stream of nitrogen, then sterols were silylated with 50 µL Tri-Sil HTP (HDMS:TMCS:Pyridine) Reagent (ThermoFisher) at 60°C for 1 hour.

Chromatography separation was performed on an Agilent gas chromatography-mass spectrometry (GC-MS) system (6890A GC and 5973 MS) (Agilent Technologies, Inc., CA, USA) with an HP-1MS capillary column (30 m length. x 250 µm diameter x 0.25 µm film thickness). The GC temperature gradient was as follows: Initial temperature of 120°C increased to 200°C at a rate of 20°C/min, then increased to 300°C at a rate of 2°C/min with a 15 minute solvent delay. Injection was at 250°C in splitless mode with ultrapurified helium as the carrier gas and the transfer line was 280°C. The mass spectra were acquired by electron impact at 70 eV using selected ion monitoring as follows: Lathosterol-TMS, cholesterol-TMS, and cholest8(9)-enol-

TMS: m/z 458; 5α-cholestane and desmosterol-TMS: m/z 372; Lanosterol-TMS: m/z 393; and 7-dehydrocholesterol-TMS: m/z 325. The data were analysed using MassHunter Workstation Quantitative Analysis Software (Agilent Technologies, Inc.) and OriginPro 2017 (OriginLab Corp, MA, USA).

Cholesterol biosynthesis assays

HeLa cell lines (described above) were seeded onto 10 cm plates and then grown in DMEM supplemented with 10% LPDS for 24 hours. Cells were washed and then incubated with 10µCi/ml [^{3}H]-acetate or 5µCi/ml [^{3}H]-mevalonate (Perkin Elmer) in the presence of 10% LPDS for another 24 hours. Cellular lipids were extracted with hexane and then evaporated to dryness. Cell lysates were produced by addition of 0.1N NaOH for 1 hour. Free cholesterol was separated by TLC in a hexane:diethyl ether:methanol:acetic acid (80:20:3:1.5) solvent system. TLC plates were obtained from Analtech, Newark, NJ. Bands corresponding to free cholesterol were scraped from the TLC plate, and radioactivity was determined by scintillation counting in a Beckman Coulter LS6500 Scintillation Counter using BetaMax ES Liquid Scintillation Cocktail (ThermoFisher).

Molecular dynamics

Simulations were constructed as previously described, starting from a modified version of the OSBPL2 lipid-binding domain structure (PDB 5ZM8)(Wang et al., 2019). Parameters for lathosterol were obtained by modifying those of cholesterol to substituting the double bond between C5-C6 with one between C7-C8. Simulations were performed with the CHARMM36 force field.

Western blotting

Cell lysates were made with a buffer containing 150mM NaCl, 0.5% Triton-X-100 and EDTA-free protease-inhibitor solution (Expedeon), 50mM Tris, pH=7.4. Cell lysates and input samples from BioID and immunoprecipitation experiments were

combined 1:1 with a 2x reducing loading buffer; a reducing loading buffer containing 10mM EDTA was added directly to Dynabead samples. SDS–PAGE and Western blotting were carried out according to standard methods.

ACKNOWLEDGEMENTS

We thank the Warburg Micro syndrome children and their families. We thank Professor C. A. Johnson and Dr J. A. Poulter for a critical reading of the manuscript and Professor Jia-Wei Wu for sharing structural data.

COMPETING INTERESTS

No competing interests declared.

FUNDING

MH is supported by the University of Leeds and by a Programme Grant from the Newlife Foundation for Disabled Children (Grant Reference Number: 17-18/23).

DATA AVAILABILITY

The mass spectrometry proteomics data have been deposited to the ProteomeXchange Consortium via the PRIDE (Perez-Riverol et al., 2019) partner repository with the dataset identifiers PXD016631, PXD016336, PXD016326, PXD016233 and PXD016404.

REFERENCES

Aligianis IA, Johnson CA, Gissen P, Chen D, Hampshire D, Hoffmann K, Maina EN, Morgan NV, Tee L, Morton J, Ainsworth JR, Horn D, Rosser E, Cole TR, Stolte-Dijkstra I, Fieggen K, Clayton-Smith J, Megarbane A, Shield JP, Newbury-Ecob R et al. (2005) Mutations of the catalytic subunit of RAB3GAP cause Warburg Micro syndrome. *Nat Genet* 37: 221-3

Anderson R, Rust S, Ashworth J, Clayton-Smith J, Taylor RL, Clayton PT, Morris AAM (2019) Lathosterolosis: A Relatively Mild Case with Cataracts and Learning Difficulties. *JIMD Rep* 44: 79-84

Angebault C, Fauconnier J, Patergnani S, Rieusset J, Danese A, Affortit CA, Jagodzinska J, Megy C, Quiles M, Cazevieille C, Korchagina J, Bonnet-Wersinger D, Milea D, Hamel C, Pinton P, Thiry M, Lacampagne A, Delprat B, Delettre C (2018) ER-mitochondria cross-talk is regulated by the Ca(2+) sensor NCS1 and is impaired in Wolfram syndrome. *Sci Signal* 11

Antonny B, Bigay J, Mesmin B (2018) The Oxysterol-Binding Protein Cycle: Burning Off PI(4)P to Transport Cholesterol. *Annu Rev Biochem* 87: 809-837

Baple E, Crosby A (2004) Troyer Syndrome. In *GeneReviews((R))*, Adam MP, Ardinger HH, Pagon RA, Wallace SE, Bean LJH, Stephens K, Amemiya A (eds) Seattle (WA):

Barr F, Lambright DG (2010) Rab GEFs and GAPs. *Curr Opin Cell Biol* 22: 461-70

Bekbulat F, Schmitt D, Feldmann A, Huesmann H, Eimer S, Juretschke T, Beli P, Behl C, Kern A (2018) RAB18 impacts autophagy via lipid droplet-derived lipid transfer and is rescued by ATG9A. *bioRxiv*: 421677

Bem D, Yoshimura S, Nunes-Bastos R, Bond FC, Kurian MA, Rahman F, Handley MT, Hadzhiev Y, Masood I, Straatman-Iwanowska AA, Cullinane AR, McNeill A, Pasha SS, Kirby GA, Foster K, Ahmed Z, Morton JE, Williams D, Graham JM, Dobyns WB et al. (2011) Loss-of-function mutations in RAB18 cause Warburg micro syndrome. *Am J Hum Genet* 88: 499-507

Blassberg R, Macrae JI, Briscoe J, Jacob J (2016) Reduced cholesterol levels impair Smoothened activation in Smith-Lemli-Opitz syndrome. *Hum Mol Genet* 25: 693-705

Borck G, Wunram H, Steiert A, Volk AE, Korber F, Roters S, Herkenrath P, Wollnik B, Morris-Rosendahl DJ, Kubisch C (2011) A homozygous RAB3GAP2 mutation causes Warburg Micro syndrome. *Human genetics* 129: 45-50

Branon TC, Bosch JA, Sanchez AD, Udeshi ND, Svinkina T, Carr SA, Feldman JL, Perrimon N, Ting AY (2018) Efficient proximity labeling in living cells and organisms with TurboID. *Nat Biotechnol* 36: 880-887

Brunet S, Saint-Dic D, Milev MP, Nilsson T, Sacher M (2016) The TRAPP Subunit Trs130p Interacts with the GAP Gyp6p to Mediate Ypt6p Dynamics at the Late Golgi. *Front Cell Dev Biol* 4: 48

Brunetti-Pierri N, Corso G, Rossi M, Ferrari P, Balli F, Rivasi F, Annunziata I, Ballabio A, Russo AD, Andria G, Parenti G (2002) Lathosterolosis, a novel multiple-malformation/mental retardation syndrome due to deficiency of 3beta-hydroxysteroid-delta5-desaturase. *Am J Hum Genet* 71: 952-8

1177 Bui M, Gilady SY, Fitzsimmons RE, Benson MD, Lynes EM, Gesson K, Alto NM,
1178 Strack S, Scott JD, Simmen T (2010) Rab32 modulates apoptosis onset and
1179 mitochondria-associated membrane (MAM) properties. *The Journal of biological*
1180 *chemistry* 285: 31590-602

1181 Cai H, Reinisch K, Ferro-Novick S (2007) Coats, tethers, Rabs, and SNAREs work
1182 together to mediate the intracellular destination of a transport vesicle. *Developmental*
1183 *cell* 12: 671-82

1184 Carney DS, Davies BA, Horazdovsky BF (2006) Vps9 domain-containing proteins:
1185 activators of Rab5 GTPases from yeast to neurons. *Trends Cell Biol* 16: 27-35

1186 Carpanini SM, McKie L, Thomson D, Wright AK, Gordon SL, Roche SL, Handley MT,
1187 Morrison H, Brownstein D, Wishart TM, Cousin MA, Gillingwater TH, Aligianis IA,
1188 Jackson IJ (2014) A novel mouse model of Warburg Micro syndrome reveals roles
1189 for RAB18 in eye development and organisation of the neuronal cytoskeleton.
1190 *Disease models & mechanisms* 7: 711-22

1191 Christoforidis S, McBride HM, Burgoyne RD, Zerial M (1999) The Rab5 effector
1192 EEA1 is a core component of endosome docking. *Nature* 397: 621-5

1193 Correa-Cerro LS, Wassif CA, Kratz L, Miller GF, Munasinghe JP, Grinberg A, Fliesler
1194 SJ, Porter FD (2006) Development and characterization of a hypomorphic Smith-
1195 Lemli-Opitz syndrome mouse model and efficacy of simvastatin therapy. *Hum Mol*
1196 *Genet* 15: 839-51

1197 Cox J, Hein MY, Luber CA, Paron I, Nagaraj N, Mann M (2014) Accurate proteome-
1198 wide label-free quantification by delayed normalization and maximal peptide ratio
1199 extraction, termed MaxLFQ. *Mol Cell Proteomics* 13: 2513-26

1200 Dejgaard SY, Murshid A, Erman A, Kizilay O, Verbich D, Lodge R, Dejgaard K, Ly-
1201 Hartig TB, Pepperkok R, Simpson JC, Presley JF (2008) Rab18 and Rab43 have
1202 key roles in ER-Golgi trafficking. *J Cell Sci* 121: 2768-81

1203 Eastman SW, Yassaee M, Bieniasz PD (2009) A role for ubiquitin ligases and
1204 Spartin/SPG20 in lipid droplet turnover. *The Journal of cell biology* 184: 881-94

1205 Feldmann A, Bekbulat F, Huesmann H, Ulbrich S, Tatzelt J, Behl C, Kern A (2017)
1206 The RAB GTPase RAB18 modulates macroautophagy and proteostasis. *Biochem*
1207 *Biophys Res Commun* 486: 738-743

1208 Fliesler SJ, Peachey NS, Herron J, Hines KM, Weinstock NI, Ramachandra Rao S,
1209 Xu L (2018) Prevention of Retinal Degeneration in a Rat Model of Smith-Lemli-Opitz
1210 Syndrome. *Sci Rep* 8: 1286

1211 Fukuda M, Kanno E, Ishibashi K, Itoh T (2008) Large scale screening for novel rab
1212 effectors reveals unexpected broad Rab binding specificity. *Mol Cell Proteomics* 7:
1213 1031-42

1214 Ge L, Melville D, Zhang M, Schekman R (2013) The ER-Golgi intermediate
1215 compartment is a key membrane source for the LC3 lipidation step of
1216 autophagosome biogenesis. *Elife* 2: e00947

1217 Gerondopoulos A, Bastos RN, Yoshimura S, Anderson R, Carpanini S, Aligianis I,
1218 Handley MT, Barr FA (2014) Rab18 and a Rab18 GEF complex are required for
1219 normal ER structure. *The Journal of cell biology* 205: 707-20

1220 Gillingham AK, Bertram J, Begum F, Munro S (2019) In vivo identification of GTPase
1221 interactors by mitochondrial relocalization and proximity biotinylation. *Elife* 8

1222 Gillingham AK, Sinka R, Torres IL, Lilley KS, Munro S (2014) Toward a
1223 comprehensive map of the effectors of rab GTPases. *Developmental cell* 31: 358-73

1224 Handley M, Sheridan E (2018) RAB18 Deficiency. In *GeneReviews((R))*, Adam MP,
1225 Ardinger HH, Pagon RA, Wallace SE, Bean LJH, Stephens K, Amemiya A (eds)
1226 Seattle (WA):

1227 Handley MT, Carpanini SM, Mali GR, Sidjanin DJ, Aligianis IA, Jackson IJ,
1228 FitzPatrick DR (2015) Warburg Micro syndrome is caused by RAB18 deficiency or
1229 dysregulation. *Open biology* 5: 150047

1230 Hendershott MC, Vale RD (2014) Regulation of microtubule minus-end dynamics by
1231 CAMSAPs and Patronin. *Proc Natl Acad Sci U S A* 111: 5860-5

1232 Ho AC, Fung CW, Siu TS, Ma OC, Lam CW, Tam S, Wong VC (2014)
1233 Lathosterolosis: a disorder of cholesterol biosynthesis resembling smith-lemli-opitz
1234 syndrome. *JIMD Rep* 12: 129-34

1235 Hueschen CL, Kenny SJ, Xu K, Dumont S (2017) NuMA recruits dynein activity to
1236 microtubule minus-ends at mitosis. *Elife* 6

1237 Im YJ, Raychaudhuri S, Prinz WA, Hurley JH (2005) Structural mechanism for sterol
1238 sensing and transport by OSBP-related proteins. *Nature* 437: 154-8

1239 Jia D, Zhang JS, Li F, Wang J, Deng Z, White MA, Osborne DG, Phillips-Krawczak
1240 C, Gomez TS, Li H, Singla A, Burstein E, Billadeau DD, Rosen MK (2016) Structural
1241 and mechanistic insights into regulation of the retromer coat by TBC1d5. *Nat*
1242 *Commun* 7: 13305

1243 Jimenez-Orgaz A, Kvainickas A, Nagele H, Denner J, Eimer S, Dengjel J, Steinberg
1244 F (2018) Control of RAB7 activity and localization through the retromer-TBC1D5
1245 complex enables RAB7-dependent mitophagy. *EMBO J* 37: 235-254

1246 Jin J, Sison K, Li C, Tian R, Wnuk M, Sung HK, Jeansson M, Zhang C, Tucholska M,
1247 Jones N, Kerjaschki D, Shibuya M, Fantus IG, Nagy A, Gerber HP, Ferrara N,
1248 Pawson T, Quaggin SE (2012) Soluble FLT1 binds lipid microdomains in podocytes
1249 to control cell morphology and glomerular barrier function. *Cell* 151: 384-99

1250 Johansson M, Lehto M, Tanhuanpaa K, Cover TL, Olkkonen VM (2005) The
1251 oxysterol-binding protein homologue ORP1L interacts with Rab7 and alters
1252 functional properties of late endocytic compartments. *Mol Biol Cell* 16: 5480-92

1253 Kelley LA, Mezulis S, Yates CM, Wass MN, Sternberg MJ (2015) The Phyre2 web
1254 portal for protein modeling, prediction and analysis. *Nat Protoc* 10: 845-58

1255 Kim DI, Jensen SC, Noble KA, Kc B, Roux KH, Motamedchaboki K, Roux KJ (2016)
1256 An improved smaller biotin ligase for BioID proximity labeling. *Mol Biol Cell* 27: 1188-
1257 96

1258 Korade Z, Xu L, Harrison FE, Ahsen R, Hart SE, Folkes OM, Mirnics K, Porter NA
1259 (2014) Antioxidant supplementation ameliorates molecular deficits in Smith-Lemli-
1260 Opitz syndrome. *Biol Psychiatry* 75: 215-22

1261 Krakowiak PA, Wassif CA, Kratz L, Cozma D, Kovarova M, Harris G, Grinberg A,
1262 Yang Y, Hunter AG, Tsokos M, Kelley RI, Porter FD (2003) Lathosterolosis: an

1263 inborn error of human and murine cholesterol synthesis due to lathosterol 5-
1264 desaturase deficiency. *Hum Mol Genet* 12: 1631-41

1265 Kumar D, Golchoubian B, Belevich I, Jokitalo E, Schlaitz AL (2019) REEP3 and
1266 REEP4 determine the tubular morphology of the endoplasmic reticulum during
1267 mitosis. *Mol Biol Cell* 30: 1377-1389

1268 Lamber EP, Siedenburg AC, Barr FA (2019) Rab regulation by GEFs and GAPs
1269 during membrane traffic. *Curr Opin Cell Biol* 59: 34-39

1270 Langemeyer L, Perz A, Kummel D, Ungermann C (2018) A guanine nucleotide
1271 exchange factor (GEF) limits Rab GTPase-driven membrane fusion. *The Journal of*
1272 *biological chemistry* 293: 731-739

1273 Lees JA, Messa M, Sun EW, Wheeler H, Torta F, Wenk MR, De Camilli P, Reinisch
1274 KM (2017) Lipid transport by TMEM24 at ER-plasma membrane contacts regulates
1275 pulsatile insulin secretion. *Science* 355

1276 Li C, Luo X, Zhao S, Siu GK, Liang Y, Chan HC, Satoh A, Yu SS (2017) COPI-
1277 TRAPPII activates Rab18 and regulates its lipid droplet association. *EMBO J* 36:
1278 441-457

1279 Li D, Zhao YG, Li D, Zhao H, Huang J, Miao G, Feng D, Liu P, Li D, Zhang H (2019)
1280 The ER-Localized Protein DFCP1 Modulates ER-Lipid Droplet Contact Formation.
1281 *Cell Rep* 27: 343-358 e5

1282 Liegel RP, Handley MT, Ronchetti A, Brown S, Langemeyer L, Linford A, Chang B,
1283 Morris-Rosendahl DJ, Carpanini S, Posmyk R, Harthill V, Sheridan E, Abdel-Salam
1284 GM, Terhal PA, Faravelli F, Accorsi P, Giordano L, Pinelli L, Hartmann B, Ebert AD
1285 et al. (2013) Loss-of-function mutations in TBC1D20 cause cataracts and male
1286 infertility in blind sterile mice and Warburg micro syndrome in humans. *Am J Hum*
1287 *Genet* 93: 1001-14

1288 Lind GE, Raiborg C, Danielsen SA, Rognum TO, Thiis-Evensen E, Hoff G,
1289 Nesbakken A, Stenmark H, Lothe RA (2011) SPG20, a novel biomarker for early
1290 detection of colorectal cancer, encodes a regulator of cytokinesis. *Oncogene* 30:
1291 3967-78

1292 Liu X, Salokas K, Tamene F, Jiu Y, Weldatsadik RG, Ohman T, Varjosalo M (2018)
1293 An AP-MS- and BioID-compatible MAC-tag enables comprehensive mapping of
1294 protein interactions and subcellular localizations. *Nat Commun* 9: 1188

1295 Martin S, Driessen K, Nixon SJ, Zerial M, Parton RG (2005) Regulated localization of
1296 Rab18 to lipid droplets: effects of lipolytic stimulation and inhibition of lipid droplet
1297 catabolism. *The Journal of biological chemistry* 280: 42325-35

1298 Nakamura H, Yamashita N, Kimura A, Kimura Y, Hirano H, Makihara H, Kawamoto
1299 Y, Jitsuki-Takahashi A, Yonezaki K, Takase K, Miyazaki T, Nakamura F, Tanaka F,
1300 Goshima Y (2016) Comprehensive behavioral study and proteomic analyses of
1301 CRMP2-deficient mice. *Genes Cells* 21: 1059-1079

1302 Nicholson JM, Macedo JC, Mattingly AJ, Wangsa D, Camps J, Lima V, Gomes AM,
1303 Doria S, Ried T, Logarinho E, Cimini D (2015) Chromosome mis-segregation and
1304 cytokinesis failure in trisomic human cells. *Elife* 4

1305 Nowaczyk MJM, Wassif CA (1998) Smith-Lemli-Opitz Syndrome. In
1306 *GeneReviews((R))*, Adam MP, Ardinger HH, Pagon RA, Wallace SE, Bean LJH,
1307 Stephens K, Amemiya A (eds) Seattle (WA):

1308 Ong WY, Ng MP, Loke SY, Jin S, Wu YJ, Tanaka K, Wong PT (2013)
1309 Comprehensive gene expression profiling reveals synergistic functional networks in
1310 cerebral vessels after hypertension or hypercholesterolemia. *PloS one* 8: e68335

1311 Ozeki S, Cheng J, Tauchi-Sato K, Hatano N, Taniguchi H, Fujimoto T (2005) Rab18
1312 localizes to lipid droplets and induces their close apposition to the endoplasmic
1313 reticulum-derived membrane. *J Cell Sci* 118: 2601-11

1314 Perez-Riverol Y, Csordas A, Bai J, Bernal-Llinares M, Hewapathirana S, Kundu DJ,
1315 Inuganti A, Griss J, Mayer G, Eisenacher M, Perez E, Uszkoreit J, Pfeuffer J,
1316 Sachsenberg T, Yilmaz S, Tiwary S, Cox J, Audain E, Walzer M, Jarnuczak AF et al.
1317 (2019) The PRIDE database and related tools and resources in 2019: improving
1318 support for quantification data. *Nucleic Acids Res* 47: D442-D450

1319 Petkovic M, Jemaiel A, Daste F, Specht CG, Izeddin I, Vorkel D, Verbavatz JM,
1320 Darzacq X, Triller A, Pfenninger KH, Tareste D, Jackson CL, Galli T (2014) The
1321 SNARE Sec22b has a non-fusogenic function in plasma membrane expansion. *Nat*
1322 *Cell Biol* 16: 434-44

1323 Platt FM, Wassif C, Colaco A, Dardis A, Lloyd-Evans E, Bembi B, Porter FD (2014)
1324 Disorders of cholesterol metabolism and their unanticipated convergent mechanisms
1325 of disease. *Annu Rev Genomics Hum Genet* 15: 173-94

1326 Pulido MR, Diaz-Ruiz A, Jimenez-Gomez Y, Garcia-Navarro S, Gracia-Navarro F,
1327 Tinahones F, Lopez-Miranda J, Fruhbeck G, Vazquez-Martinez R, Malagon MM
1328 (2011) Rab18 dynamics in adipocytes in relation to lipogenesis, lipolysis and obesity.
1329 *PloS one* 6: e22931

1330 Raiborg C, Wenzel EM, Pedersen NM, Olsvik H, Schink KO, Schultz SW, Vietri M,
1331 Nisi V, Bucci C, Brech A, Johansen T, Stenmark H (2015) Repeated ER-endosome
1332 contacts promote endosome translocation and neurite outgrowth. *Nature* 520: 234-8

1333 Ran FA, Hsu PD, Wright J, Agarwala V, Scott DA, Zhang F (2013) Genome
1334 engineering using the CRISPR-Cas9 system. *Nat Protoc* 8: 2281-2308

1335 Richter KN, Revelo NH, Seitz KJ, Helm MS, Sarkar D, Saleeb RS, D'Este E, Eberle
1336 J, Wagner E, Vogl C, Lazaro DF, Richter F, Coy-Vergara J, Coceano G, Boyden ES,
1337 Duncan RR, Hell SW, Lauterbach MA, Lehnart SE, Moser T et al. (2018) Glyoxal as
1338 an alternative fixative to formaldehyde in immunostaining and super-resolution
1339 microscopy. *EMBO J* 37: 139-159

1340 Rocha N, Kuijl C, van der Kant R, Janssen L, Houben D, Janssen H, Zwart W,
1341 Neefjes J (2009) Cholesterol sensor ORP1L contacts the ER protein VAP to control
1342 Rab7-RILP-p150 Glued and late endosome positioning. *The Journal of cell biology*
1343 185: 1209-25

1344 Rossi M, D'Armiento M, Parisi I, Ferrari P, Hall CM, Cervasio M, Rivasi F, Balli F,
1345 Vecchione R, Corso G, Andria G, Parenti G (2007) Clinical phenotype of
1346 lathosterolosis. *Am J Med Genet A* 143A: 2371-81

1347 Roux KJ, Kim DI, Burke B, May DG (2018) BioID: A Screen for Protein-Protein
1348 Interactions. *Curr Protoc Protein Sci* 91: 19 23 1-19 23 15

1349 Roux KJ, Kim DI, Raida M, Burke B (2012) A promiscuous biotin ligase fusion
1350 protein identifies proximal and interacting proteins in mammalian cells. *The Journal*
1351 *of cell biology* 196: 801-10

1352 Schlaitz AL, Thompson J, Wong CC, Yates JR, 3rd, Heald R (2013) REEP3/4
1353 ensure endoplasmic reticulum clearance from metaphase chromatin and proper
1354 nuclear envelope architecture. *Developmental cell* 26: 315-23

1355 Seaman MN, Harbour ME, Tattersall D, Read E, Bright N (2009) Membrane
1356 recruitment of the cargo-selective retromer subcomplex is catalysed by the small
1357 GTPase Rab7 and inhibited by the Rab-GAP TBC1D5. *J Cell Sci* 122: 2371-82

1358 Sidjanin DJ, Park AK, Ronchetti A, Martins J, Jackson WT (2016) TBC1D20
1359 mediates autophagy as a key regulator of autophagosome maturation. *Autophagy*: 1-
1360 17

1361 Silve S, Dupuy PH, Labit-Lebouteiller C, Kaghad M, Chalon P, Rahier A, Taton M,
1362 Lupker J, Shire D, Loison G (1996) Emopamil-binding protein, a mammalian protein
1363 that binds a series of structurally diverse neuroprotective agents, exhibits delta8-
1364 delta7 sterol isomerase activity in yeast. *The Journal of biological chemistry* 271:
1365 22434-40

1366 Sobajima T, Yoshimura SI, Maeda T, Miyata H, Miyoshi E, Harada A (2018) The
1367 Rab11-binding protein RELCH/KIAA1468 controls intracellular cholesterol
1368 distribution. *The Journal of cell biology* 217: 1777-1796

1369 Spang A (2012) The DSL1 complex: the smallest but not the least CATCHR. *Traffic*
1370 13: 908-13

1371 Spang N, Feldmann A, Huesmann H, Bekbulat F, Schmitt V, Hiebel C, Koziollek-
1372 Drechsler I, Clement AM, Moosmann B, Jung J, Behrends C, Dikic I, Kern A, Behl C
1373 (2014) RAB3GAP1 and RAB3GAP2 modulate basal and rapamycin-induced
1374 autophagy. *Autophagy* 10: 2297-309

1375 Svoboda MD, Christie JM, Eroglu Y, Freeman KA, Steiner RD (2012) Treatment of
1376 Smith-Lemli-Opitz syndrome and other sterol disorders. *Am J Med Genet C Semin*
1377 *Med Genet* 160C: 285-94

1378 Tagaya M, Arasaki K, Inoue H, Kimura H (2014) Moonlighting functions of the NRZ
1379 (mammalian Dsl1) complex. *Front Cell Dev Biol* 2: 25

1380 Tinti M, Johnson C, Toth R, Ferrier DE, Mackintosh C (2012) Evolution of signal
1381 multiplexing by 14-3-3-binding 2R-ohnologue protein families in the vertebrates.
1382 *Open biology* 2: 120103

1383 Urnavicius L, Zhang K, Diamant AG, Motz C, Schlager MA, Yu M, Patel NA,
1384 Robinson CV, Carter AP (2015) The structure of the dynactin complex and its
1385 interaction with dynein. *Science* 347: 1441-1446

1386 Vazquez-Martinez R, Cruz-Garcia D, Duran-Prado M, Peinado JR, Castano JP,
1387 Malagon MM (2007) Rab18 inhibits secretory activity in neuroendocrine cells by
1388 interacting with secretory granules. *Traffic* 8: 867-82

1389 Wang H, Ma Q, Qi Y, Dong J, Du X, Rae J, Wang J, Wu WF, Brown AJ, Parton RG,
1390 Wu JW, Yang H (2019) ORP2 Delivers Cholesterol to the Plasma Membrane in
1391 Exchange for Phosphatidylinositol 4, 5-Bisphosphate (PI(4,5)P2). *Mol Cell* 73: 458-
1392 473 e7

1393 Wang T, Li L, Hong W (2017) SNARE proteins in membrane trafficking. *Traffic* 18:
1394 767-775

1395 Wassif CA, Kratz L, Sparks SE, Wheeler C, Bianconi S, Gropman A, Calis KA,
1396 Kelley RI, Tierney E, Porter FD (2017) A placebo-controlled trial of simvastatin
1397 therapy in Smith-Lemli-Opitz syndrome. *Genet Med* 19: 297-305

1398 Whitfield ST, Burston HE, Bean BD, Raghuram N, Maldonado-Baez L, Davey M,
1399 Wendland B, Conibear E (2016) The alternate AP-1 adaptor subunit Apm2 interacts
1400 with the Mil1 regulatory protein and confers differential cargo sorting. *Mol Biol Cell*
1401 27: 588-98

1402 Wickner W (2010) Membrane fusion: five lipids, four SNAREs, three chaperones,
1403 two nucleotides, and a Rab, all dancing in a ring on yeast vacuoles. *Annu Rev Cell*
1404 *Dev Biol* 26: 115-36

1405 Williams C, Choudhury R, McKenzie E, Lowe M (2007) Targeting of the type II
1406 inositol polyphosphate 5-phosphatase INPP5B to the early secretory pathway. *J Cell*
1407 *Sci* 120: 3941-51

1408 Wu H, Carvalho P, Voeltz GK (2018) Here, there, and everywhere: The importance
1409 of ER membrane contact sites. *Science* 361

1410 Xu D, Li Y, Wu L, Li Y, Zhao D, Yu J, Huang T, Ferguson C, Parton RG, Yang H, Li
1411 P (2018) Rab18 promotes lipid droplet (LD) growth by tethering the ER to LDs
1412 through SNARE and NRZ interactions. *The Journal of cell biology* 217: 975-995

1413 Yamamoto Y, Yurugi C, Sakisaka T (2017) The number of the C-terminal
1414 transmembrane domains has the potency to specify subcellular localization of
1415 Sec22c. *Biochem Biophys Res Commun* 487: 388-395

1416 Zhang T, Wong SH, Tang BL, Xu Y, Hong W (1999) Morphological and functional
1417 association of Sec22b/ERS-24 with the pre-Golgi intermediate compartment. *Mol*
1418 *Biol Cell* 10: 435-53

1419 Zhao K, Ridgway ND (2017) Oxysterol-Binding Protein-Related Protein 1L Regulates
1420 Cholesterol Egress from the Endo-Lysosomal System. *Cell Rep* 19: 1807-1818

1421 Zhao L, Imperiale MJ (2017) Identification of Rab18 as an Essential Host Factor for
1422 BK Polyomavirus Infection Using a Whole-Genome RNA Interference Screen.
1423 *mSphere* 2

1424 Zhen Y, Stenmark H (2015) Cellular functions of Rab GTPases at a glance. *J Cell*
1425 *Sci* 128: 3171-6

1426

1427

A

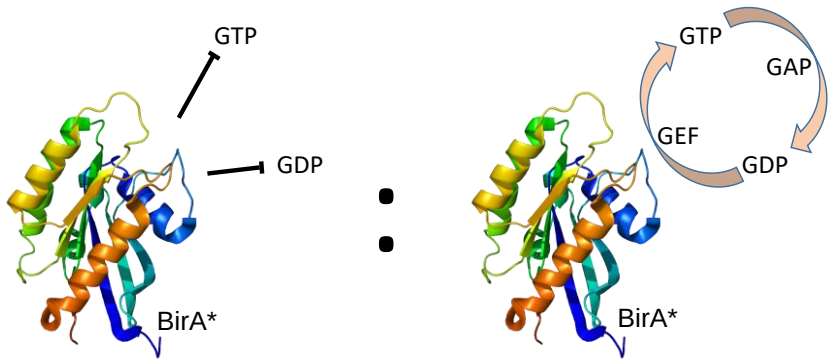

B

Protein	Ratio	Orthologue PPI (Gillingham et al., 2014)	Additional evidence	
SCFD2	0.00	Slh	Gillingham et al., 2019	RAB3GAP-dependent association in HeLa cells
ZW10	0.00	mit(1)15	Xu et al., 2018; Gillingham et al., 2019	
NBAS	0.00	rod	Xu et al., 2018; Gillingham et al., 2019	
CAMSAP1	0.04			
FAM134B	0.36			
RINT1	0.41	CG8605	Xu et al., 2018	
RAB3GAP2	1.58	rab3-GAP	Gerondopoulos et al., 2014	
RAB3GAP1	1.59	CG31935	Gerondopoulos et al., 2014	
TBC1D5	0.00	CG8449	Gillingham et al., 2019	TRAPPII-dependent association in HeLa cells
c15orf38	0.00			
SEC23IP	0.00			
ATP6AP2	0.29			
GORASP2	0.36			
GIGYF2	0.41			
TPR	0.41			
USP15	0.00			Present in HeLa dataset (n≥2)
TMPO	0.00			
ARFGAP3	0.20			
ARFGAP2	0.31			
SLK	0.34			
NUP153	0.39			
ATG2B	0.43			
SCFD1	0.45	Slh	Gillingham et al., 2019	
USE1	0.45		Xu et al., 2018	
TMX1	0.45			
CORO1B	0.47			
PREB	0.47			
SLC25A4	0.00			Absent in HeLa dataset (n≥2)
LUZP1	0.00			
DPYSL2	0.34		Nakamura et al., 2016	

Figure 1. Nucleotide-binding-dependent RAB18-associations in HEK293 cells. (A) Schematic to show BirA*-RAB18(Ser22Asn):BirA*-RAB18(WT) comparison. RAB18 crystal structure from RCSB PDB code 1X3S. (B) Table to show putative nucleotide-binding-dependent RAB18-associations with BirA*-RAB18(Ser22Asn):BirA*-RAB18(WT) association ratios <0.5. Proteins orthologous to interactors identified by Gillingham et al. (2014) are indicated. Previous studies providing supporting evidence for interactions are indicated. Proteins are grouped according to their attributes in the HeLa cell dataset (Figure 2 and Table S2). Association ratios were derived individually following normalization by total spectral counts per condition. The full dataset is provided in table S1.

A

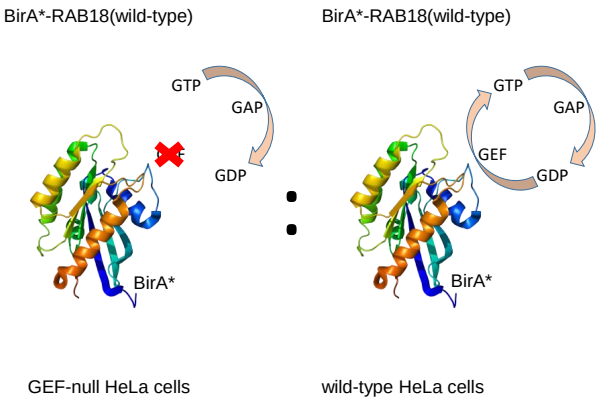

B

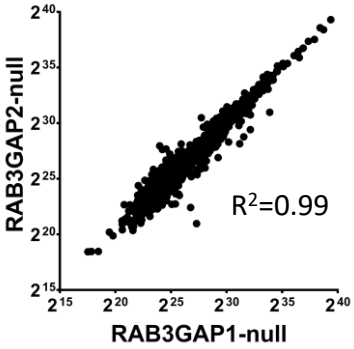

C

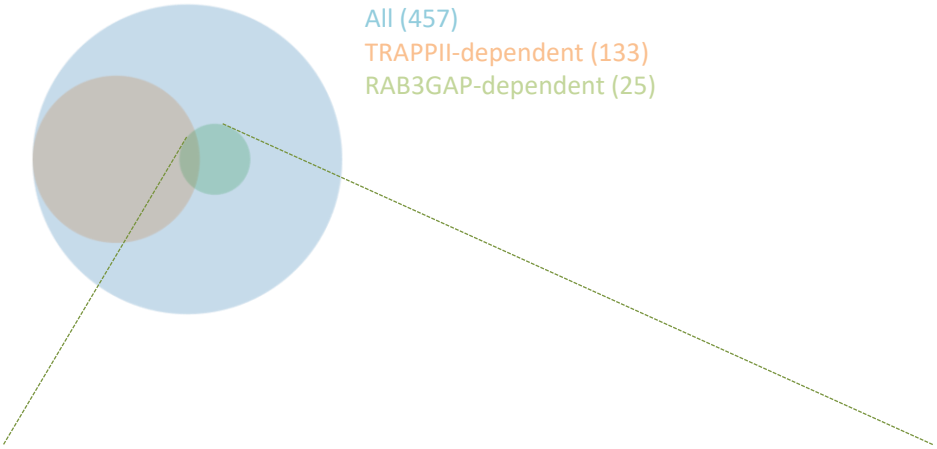

D

Protein	n	Ratio	Orthologue PPI (Gillingham et al., 2014)	Additional evidence	
CAMSAP1	3	0.26			
REEP4	3	0.35		Tinti et al., 2012*	**Microtubule-associated/Membrane remodelling**
BICD2	2	0.25	BicD	Gillingham et al., 2019	
SPG20	**2**	**0.42**	**CG12001**	**This study (Figure 4)**	
FAM134B	2	0.46			
ZW10	3	0.02	mit(1)15	Xu et al., 2018; Gillingham et al., 2019	
RINT1	3	0.16	CG8605	Xu et al., 2018	
NBAS	3	0.17	rod	Xu et al., 2018; Gillingham et al., 2019	
SCFD2	3	0.41	Slh	Gillingham et al., 2019	**Membrane tethering/docking**
SEC22A	**3**	**0.46**		**This study (Figure 5)**	
WFS1	2	0.00			
BNIP1	2	0.36		Xu et al., 2018	
STX18	2	0.40	Syx18	Xu et al., 2018	
TMCO4	**3**	**0.06**		**This study (Figure 6)**	
OSBPL2	**3**	**0.35**		**This study (Figure 7)**	
EBP	**3**	**0.38**		**This study (Figure 7)**	**Lipid modifying/ mobilising**
INPP5B	**2**	**0.00**		**This study (Figure 7)**	
C2CD2L	2	0.22			
C2CD2	2	0.36			
RAB3GAP2	3	0.00	rab3-GAP	Gerondopoulos et al., 2014	
RAB3GAP1	3	0.01	CG31935	Gerondopoulos et al., 2014	
SSR3	3	0.49			**Other**
MFHAS1	2	0.00	Irrk		
TRIM13	2	0.29			
SCARA3	2	0.42			

Figure 2. RAB3GAP-dependent RAB18-associations in HeLa cells. (A) Schematic to show comparison of BirA*-RAB18(WT) in wild-type and guanine nucleotide exchange factor (GEF)-null cells. RAB18 crystal structure from RCSB PDB code 1X3S. (B) Plot to show correlation between non-zero LFQ intensities of individual proteins identified in samples purified from RAB3GAP1- and RAB3GAP2-null cells. (C) Venn diagram illustrating all RAB18-associations, TRAPPII-dependent interactions (TRAPPC9-null:wild-type association ratios <0.5) and RAB3GAP-dependent associations (RAB3GAP1/2-null:wild-type association ratios <0.5). (D) Table to show putative RAB18-associations with RAB3GAP1/2-null:wild-type association ratios <0.5. Proteins orthologous to interactors identified by Gillingham et al. (2014) are indicated. Previous studies providing supporting evidence for interactions are indicated. Proteins are grouped according to their reported functions. Association ratios were derived individually following normalization by RAB18 LFQ intensity in each replicate experiment. The full dataset is provided in table S2.

A

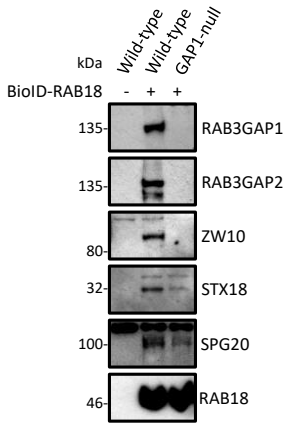

B

Gene	Homologue	Syndrome	Inheritance	OMIM	Overlapping features
SPG20	-	Troyer syndrome (SPG20)	AR	275900	ascending spastic paraplegia, postnatal microcephaly, intellectual disability
BICD2	-	Spinal muscular atrophy	AD	615290; 615291	ascending spastic paraplegia, lower muscle atrophy
REEP4	*REEP1*	SPG31	AD	610250	ascending spastic paraplegia
REEP4	*REEP2*	SPG72	AD	615625	ascending spastic paraplegia
FAM134B	-	HSAN IIB	AR	613115	neuropathy
EBP	-	CDPX2; MEND syndrome	XLD; XLR	302960; 300960	cataract, microphthalmia, microcornea, intellectual disability, hypotonia, seizures, corpus callosum hypogenesis, cerebellar vermis hypoplasia, micrognathia, cryptorchidism
WFS1	-	Wolfram syndrome; CTRCT41	AR; AD	222300; 116400	cataract, optic atrophy, hypogonadism, short stature; congenital cataract
INPP5B	*OCRL*	Lowe syndrome	XLR	309000	cataract, intellectual disability
INPP5B	*INPP5K*	MDCCAID	AR	607875	cataract, intellectual disability, microcephaly, spasticity, seizures
NBAS	-	SOPH syndrome	AR	614800	short stature, optic atrophy

C

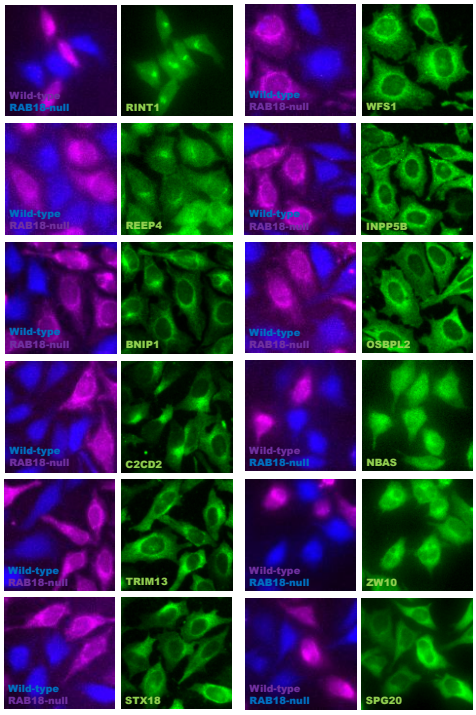

D

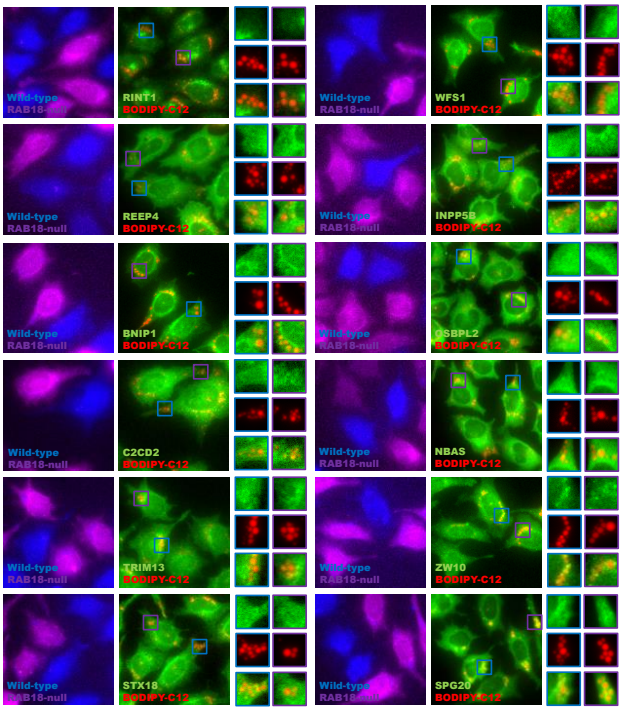

Figure 3. Initial validation of RAB3GAP-dependent RAB18-associations in HeLa cells. (A) Western blotting of samples purified from wild-type and RAB3GAP1-null cells in an independent BioID experiment. Levels of selected proteins are consistent with association ratios in Figure 1C. (B) Table to show diseases with features overlapping those of Warburg Micro syndrome linked to genes encoding putative effector proteins or their homologues. (C) Comparative fluorescence microscopy of selected RAB18-associated proteins in wild-type and RAB18-null HeLa cells. Cells of different genotypes were labelled with CellTrace-Violet and CellTrace-Far Red reagents, corresponding to blue and magenta channels respectively. Cells were stained with antibodies against indicated proteins in green

1468 channel panels. (D) Comparative fluorescence microscopy of selected RAB18-
1469 associated proteins in lipid-loaded wild-type and RAB18-null HeLa cells. Cells were
1470 stained as above but were treated for 15 hours with 200µM oleic acid, 1µg/ml
1471 BODIPY-558/568-C12 (Red channel) prior to fixation.
1472

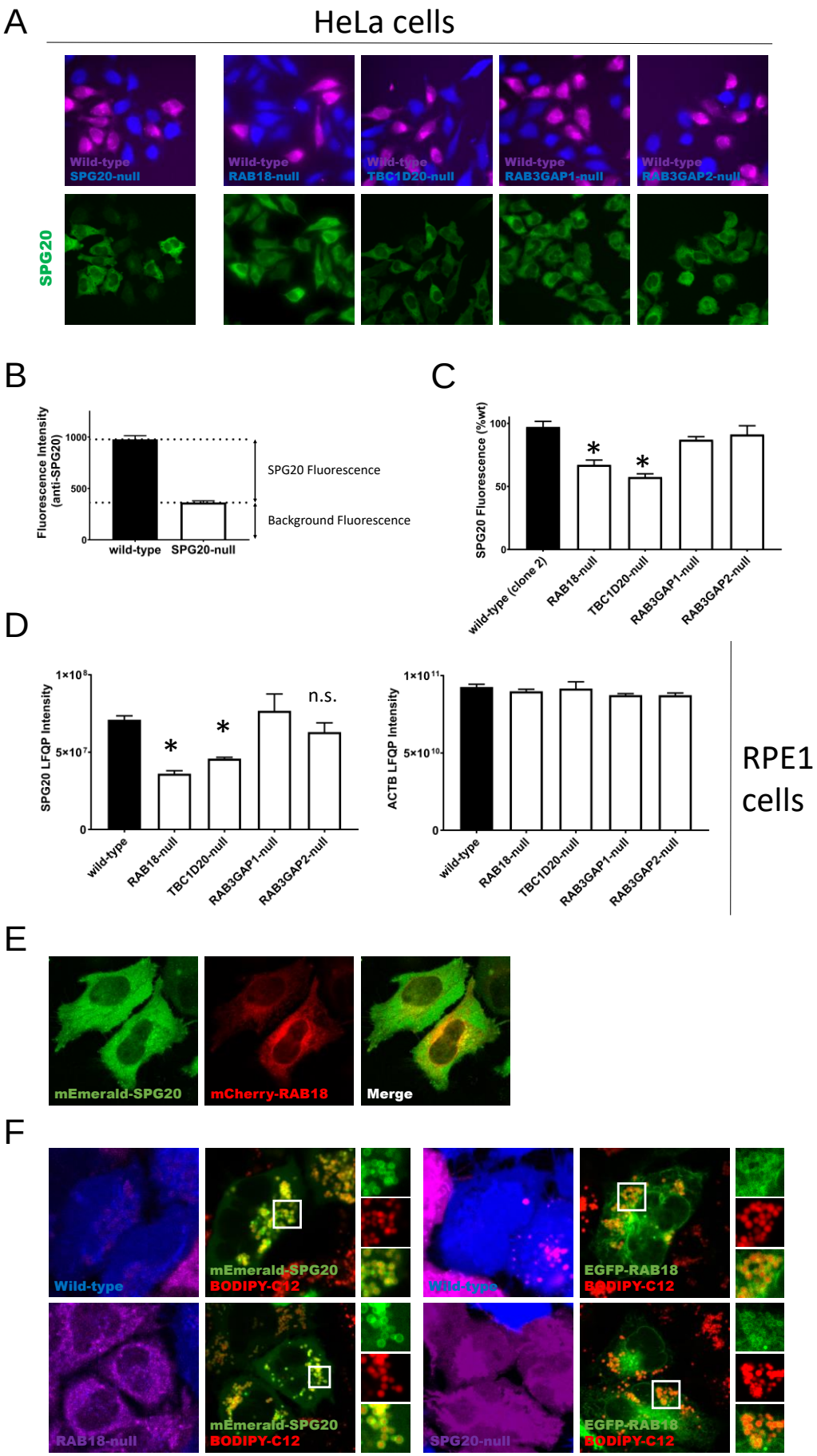

Figure 4. Levels of SPG20 are significantly reduced in RAB18-null and TBC1D20-null HeLa and RPE1 cells. (A) Comparative fluorescence microscopy of SPG20 in wild-type and mutant HeLa cell lines. Wild-type and mutant cells of the indicated genotypes were labelled with CellTrace-Far Red and CellTrace-Violet and reagents respectively (magenta and blue channels). Cells were stained with an antibody against SPG20 (green channel) (B) Quantification of SPG20 fluorescence in wild-type cells by direct comparison with SPG20-null cells. (C) Quantification of SPG20 fluorescence (%wt) in cells of different genotypes. Data were derived from analysis of at least 18 frames – each containing >5 wild-type and >5 mutant cells – per genotype. *p<0.001. (D) LFQ intensities for SPG20 (Q8N0X7) and β-Actin (P60709) in whole-cell lysates of RPE1 cells of the indicated genotypes. n=3; *p<0.05 following FDR correction. Full dataset provided in table S3. Error bars represent s.e.m. (E) Confocal micrograph to show localization of exogenous mEmerald-SPG20 (Green) and mCherry-RAB18 (Red) in HeLa cells. (F) Confocal micrographs to show localization of exogenous mEmerald-SPG20 (Green; left panels) and EGFP-RAB18 (Green; right panels) in HeLa cells loaded with 200µM oleic acid, 1µg/ml BODIPY-558/568-C12 (Red channel). Wild-type and mutant cells of the indicated genotypes were labelled with CellTrace-Violet and CellTrace-Far Red reagents respectively (magenta and blue channels).

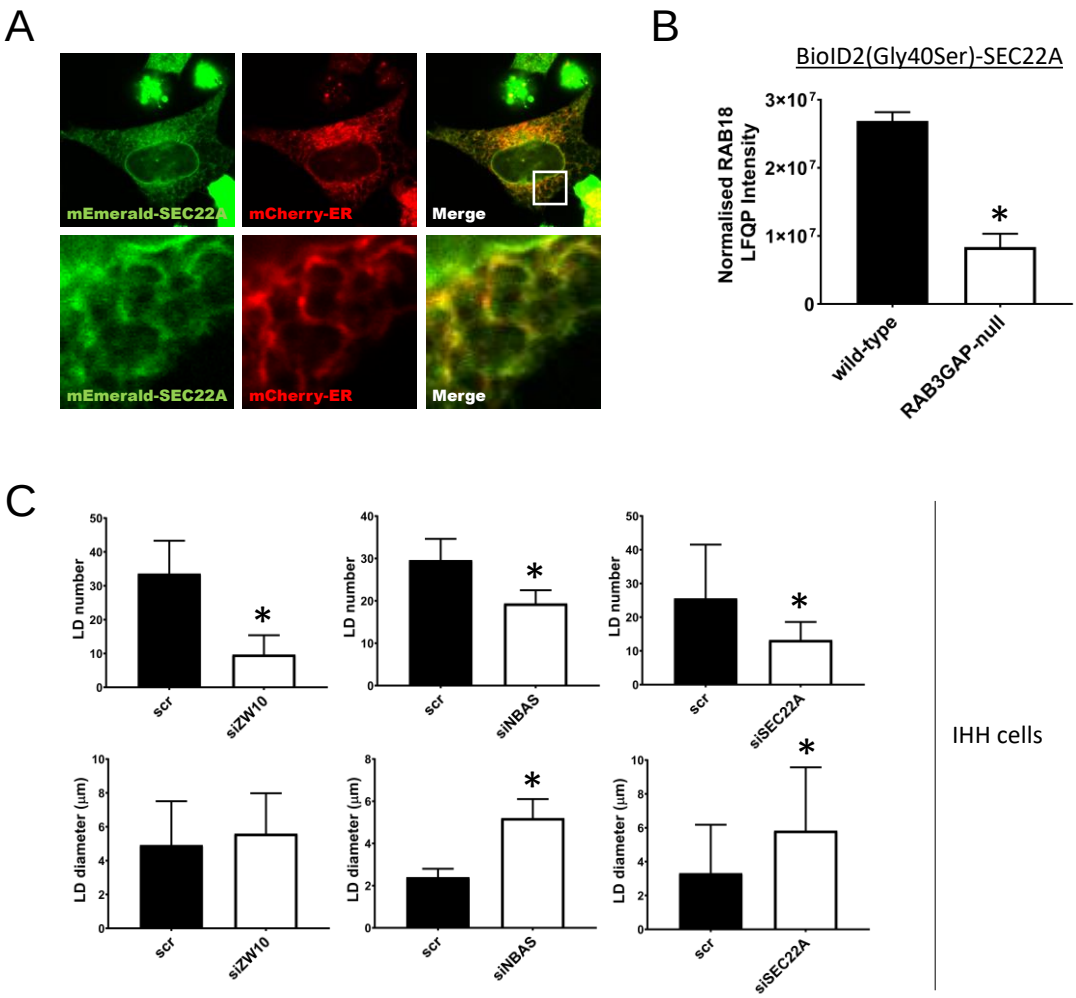

Figure 5. SEC22A associates with RAB18 and influences LD morphology. (A) Confocal micrograph to show overlapping localization of exogenous mEmerald-SEC22A (Green) and mCherry-ER (Red) in HeLa cells. (B) RAB18 LFQ intensities from a reciprocal BioID experiment showing a reduced association between BioID2(Gly40Ser)-SEC22A and endogenous RAB18 in RAB3GAP-null compared to wild-type HeLa cells. Data were adjusted to account for non-specific binding of RAB18 to beads and normalized by SEC22A LFQ intensities in each replicate experiment. Error bars represent s.e.m. Data for other BioID2(Gly40Ser)-SEC22A-associated proteins are provided in table S5. (C) Bar graphs to show effects of ZW10, NBAS and SEC22A knockdowns on lipid droplet number and diameter. siRNA-treated IHH cells were loaded with 200nM BSA-conjugated oleate, fixed and stained with BODIPY and DAPI, and imaged. Images were analysed using ImageJ. Data are derived from measurements from >100 cells/condition and are representative of three independent experiments. Error bars represent SD. *p<0.001

A

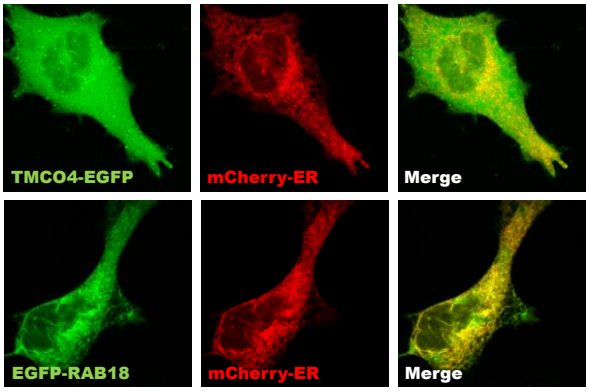

B

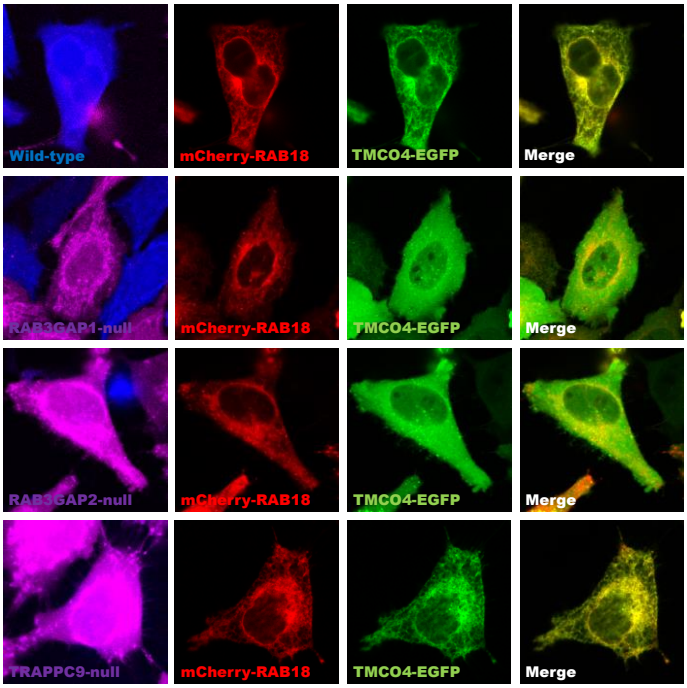

C

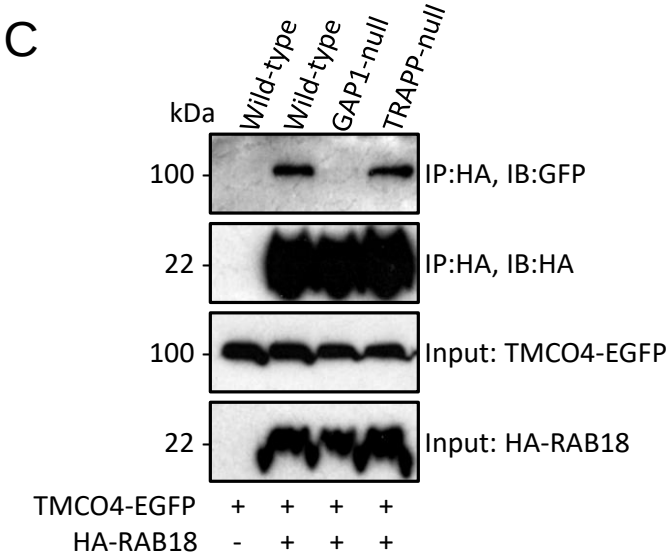

Figure 6. mCherry-RAB18 recruits TMCO4-EGFP to the ER membrane in a RAB3GAP-dependent manner. (A) Confocal micrographs to show diffuse localization of exogenous TMCO4-EGFP (Green) compared to mCherry-ER (Red) and overlapping localization of exogenous EGFP-RAB18 (Green) and mCherry-ER in HeLa cells. (B) Confocal micrographs to show localization of exogenous mCherry-RAB18 and TMCO4-EGFP in wild-type cells and in mutant cells of different genotypes. Wild-type and mutant cells of the indicated genotypes were labelled with CellTrace-Violet and CellTrace-Far Red reagents respectively (magenta and blue channels). (C) Immunoprecipitation of exogenous HA-RAB18 from HeLa cells of different genotypes. Cells were transfected with the indicated constructs and lysed 24 hours post-transfection. Anti-HA immunoprecipitates and input samples were subjected to SDS-PAGE and immunostaining for HA and GFP.

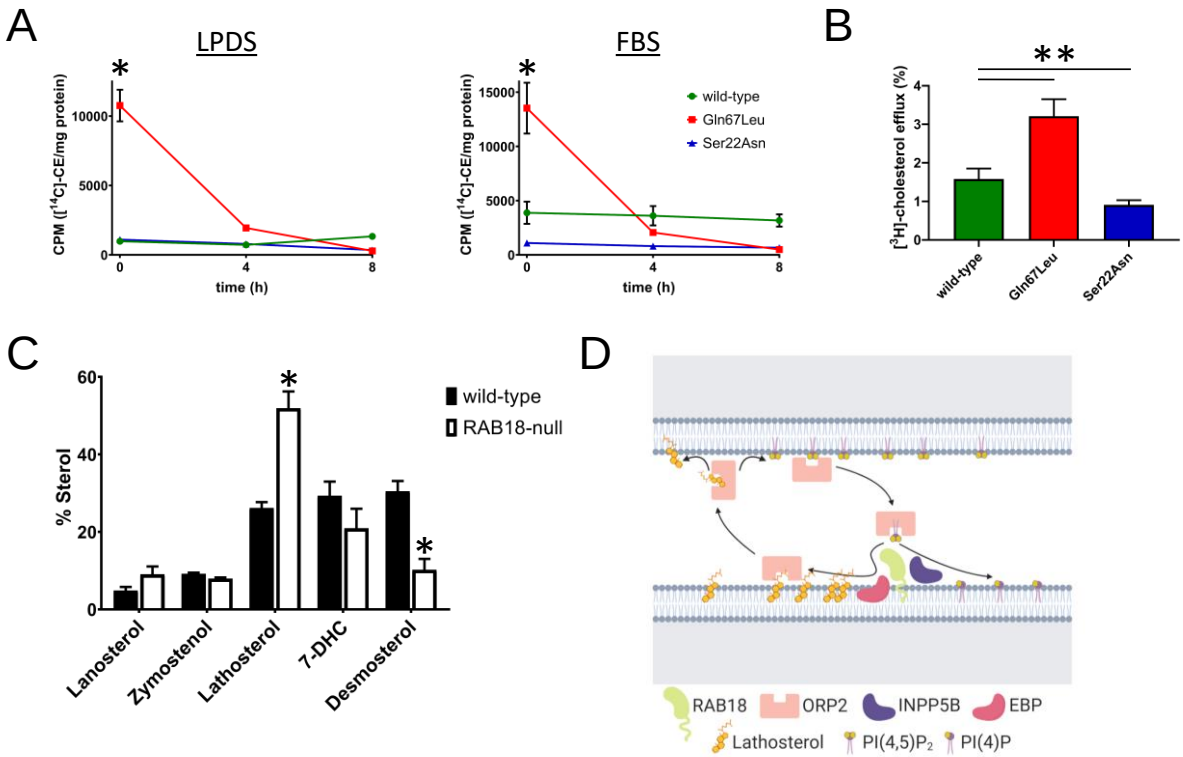

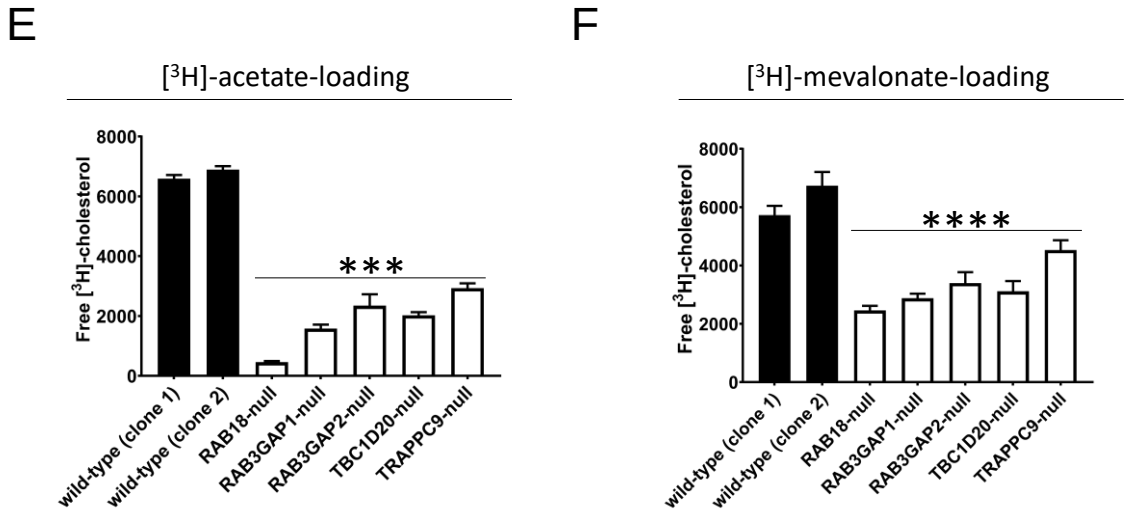

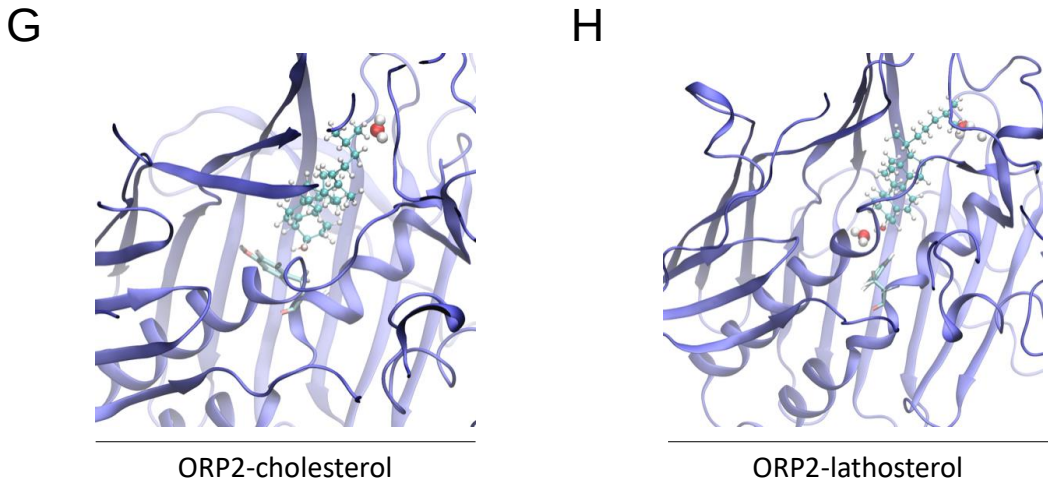

Figure 7. RAB18 is involved in the mobilization and biosynthesis of cholesterol. (A) Plots to show cholesteryl ester (CE) loading and efflux. CHO cells, stably expressing RAB18(WT), RAB18(Gln67Leu) and RAB18(Ser22Asn), were incubated with [^{14}C]-oleate, for 24 hours, in the presence of lipoprotein depleted serum (LPDS)(Left panel) or FBS (Right panel). Following lipid extraction, thin layer chromatography (TLC) was used to separate CE, and radioactivity was measured by scintillation counting. Measurements were made at t=0 and at 4 and 8 hours following the addition of 50µg/ml high density lipoprotein (HDL) to the cells. (B) Bar graph to show cholesterol efflux. The CHO cells were incubated with [^{3}H]-cholesterol, for 24 hours, in the presence of FBS. After washing, they were then incubated with 25µg/ml apolipoprotein A-I for 5 hours. The quantity of [^{3}H]-cholesterol in the media is shown as a percentage of the total cellular radioactivity (mean+/-SD). (C) Bar graph to show sterols profile in wild-type and RAB18-null HeLa cells. Cells were grown in media supplemented with LPDS for 48 hours. Extracted sterols were analysed by gas chromatography-mass spectrometry (GC-MS). % Sterol was calculated as a proportion of total quantified sterols, excluding cholesterol, following normalization to a 5α-cholestane internal standard. n=3 (D) Model for lathosterol mobilization mediated by RAB18. ORP2 binds PI(4,5)P_2 on an apposed membrane. RAB18 interacts with ORP2 and INPP5B promoting the hydrolysis of PI(4,5)P_2 to PI(4)P and maintaining a PI(4,5)P_2 concentration gradient. RAB18 coordinates the production of lathosterol by EBP and its subsequent mobilization by ORP2. (E) Bar graph to show incorporation of [^{3}H]-acetate into cholesterol in a panel of HeLa cell lines. Cells were grown in LPDS-media for 24 hours then incubated with 10µCi/well [^{3}H]-acetate for 24 hours. TLC was used to separate free cholesterol and radioactivity was quantified by scintillation counting (n=4; mean±SD). (F) Bar graph to show incorporation of [^{3}H]-mevalonate into cholesterol in the cell lines. Cells were grown LPDS-media for 24 hours, then incubated with 5µCi/well [^{3}H]-mevalonate for 24 hours. TLC was used to separate free cholesterol and radioactivity was quantified by scintillation counting (n=4; mean±SD). (G) Still image from a molecular dynamics model of the ORP2 OSBP-related domain (ORD) complexed with cholesterol. Position of ORP2 Tyr110 (NP_653081) is shown. (H) Still image from a molecular dynamics model of the ORP2-ORD complexed with lathosterol. Positions of ORP2 Tyr110 and proximal water molecules are shown. *p<0.01, **p<0.001, ***p<0.0005, ****p<0.005.